CONTRIBUTIONS
OF THE ASTRONOMICAL OBSERVATORY
SKALNATÉ PLESO

• VOLUME LIV •

Number 1

February 2024

CONTENTS

3

EDITORIAL

In 2023, the journal Contributions of the Astronomical Observatory Skalnaté Pleso (CAOSP) published 9 regular articles on 126 pages within two issues, and 35 articles on 382 pages in the form of two 'Special issues'. According to the *Journal Citation Reports* database, the articles published in 2022 received 206 citations corresponding to the journal impact factor (JIF) of 0.5 and the JIF Quartile Q4.

Volume 53/1 publishes five regular articles on various topics. Individual contributions presented results on the accretion disk in the microquasar GRS 1915+105 that contains a black hole, on the radio recombination lines in the medium toward the S140 nebula, on the optimal conditions of the spacecraft acceleration in the gravitational field of a planet, and on a highly accurate analytical solutions of Keplers equation. One article was devoted to the appropriate site selection for the astronomical observatory.

Volume 53/2 published four regular articles. In the first contribution, the authors tested various methods for the identification of new small bodies, especially asteroids, in the Solar System. In the following article, the author presents a useful derivation of gravitational acceleration in a system other than the commonly used Schwarzschild coordinates. The third paper deals with the issue of aluminum abundance in A-type main sequence stars as well as in chemically peculiar Am stars. In the last article, the authors calculate the conditions under which asteroids can reach the geocentric orbit, and how long they can stay on it or collide with the Earth.

Volumes 53/3 and 53/4 introduce selected contributions based on lectures presented at the "V Meeting on Astrophysical Spectroscopy - A&M DATA: Astronomy & Earth Observations" (Palić, Serbia, September 12-15, 2023) and at the "18th INTEGRAL/BART Workshop" (Karlovy Vary, Czech Republic, May 22-26, 2023), respectively.

During 2023, the editorial board in cooperation with the advisory board specified the basic ethical rules of scientific publishing in CAOSP. The document can be found on the journal's website.

Tatranská Lomnica, January, 2024

Augustín Skopal, Editor-in-Chief

Richard Komžík, Managing Editor

A computer program calculating the closest approaches of asteroid to the mean orbits of meteoroid streams

M. Kováčová and L. Neslušan

Astronomical Institute of the Slovak Academy of Sciences
059 60 Tatranská Lomnica, The Slovak Republic(E-mail: mkovacova@ta3.sk)

Abstract. Meteoroid particles can collide with asteroids. If a meteoroid is large, it can trigger asteroid activity; an outburst of brightness occurs. When the meteoroids in a stream cross a region of interplanetary space, the flux of these meteoroids is considerably larger than that of sporadic meteoroids in the same region. Therefore, the probability of a collision is significantly larger there. To map the passages of a given main-belt asteroid through the known meteoroid streams, we created a computer program which calculates the characteristics of the close approaches of the asteroid to the mean orbits of known meteoroid streams. The public-domain program is available along with this article and on: https://github.com/neslusan/BELTCROSS2. It contains the executable static-binary code as well as the Fortran source code. In the article, we give a more detailed description of the program.

Key words: computer program – dynamics of meteoroid stream – main-belt asteroids – collisions between asteroids and stream meteoroids

1. Introduction

Asteroids and comets belong to the small bodies of the Solar System. In the past, it was thought that these categories were clearly distinguishable. Then objects with dynamically asteroidal orbits, but comet-like activity started to be discovered. The first such object, comet 107P/Wilson-Harrington, alternatively known as asteroid 4015 Wilson-Harrington, was discovered in 1949 (Cunningham, 1950).

This class of objects is also known as active asteroids. At the time of writing this paper, there were known about forty active main-belt asteroids. The active asteroid can be defined by (1) a semi-major axis smaller than the semi-major axis of Jupiter, (2) a Tisserand's parameter with respect to Jupiter $T_J > 3.08$ and (3) the presence of cometary features such as a coma and/or tail(s). The limit $T_J = 3.08$ (rather than the usual 3.0 for distinguishing asteroids and comets) was chosen due to the slightly eccentric orbit of Jupiter which differs from a circular orbit, which figures in the restricted 3-body problem. Thus, Encke-type comets (comet 2P/Encke has $T_J = 3.02$) and quasi-Hilda comets

($T_J \sim 2.9-3.04$) are excluded from the group of objects with $T_J > 3$ (Jewitt et al., 2015).

The activity of comets is caused by the sublimation of ice and accompanying dust removal (Whipple, 1951). In the case of active asteroids, several possible mechanisms of activity accompanied by a mass loss are discussed. For example, Hsieh et al. (2010) considered the process of ice sublimation and dust ejection as a source of activity of 133P/Elst-Pizarro (asteroidal designation 7968 Elst-Pizarro). The mechanism of rotational instability was suggested for asteroids P/2012 F5 (Gibbs) (Drahus et al., 2015) and 6478 Gault (e.g. Kleyna et al., 2019; Devogèle et al., 2021).

A meteoroid impact can also trigger an observable activity. At the first time, this mechanism was found to be the most probable mechanism to explain the activity of asteroid P/2010 A2 (Kim et al., 2017a,b). It was discovered, being already active, on January 6, 2010 by the Lincoln Near Earth Asteroid Research (LINEAR). In the case of trigerring of activity by an impact, it is more likely that this is caused by a stream meteoroid which moves around the Sun in a corridor with a relatively much higher density of meteoroids than the density of sporadic meteoroids. (The term "corridor" refers to an interplanetary space around the mean orbit of a stream. The orbits of all stream meteoroids are situated within this space.) For example, this hypothesis was applied to asteroid 596 Scheila by Neslušan et al. (2016) as an attempt to explain its activity. Instead of a fast rotation, such collisions are the most likely cause of the activity of 6478 Gault according to Ivanova et al. (2020).

Other mechanisms which can cause observable activity include the electrostatic forces, radiation pressure sweeping, and thermal fracture or dehydration (e.g. Jewitt, 2012; Jewitt et al., 2015). However, the activity of a real object may be triggered by different mechanisms operating together (Jewitt et al., 2015).

In this work, we present a tool which can help to gain some data that a researcher needs when he wants to estimate a probability that activity of an asteroid was triggered by a meteoroid impact. The probability of such the impact is high when the asteroid crosses a compact, numerous stream, since the number density of meteoroids in such the stream is larger than that in the neighboring interplanetary space. To reveal if this mechanism of the triggering of activity is relevant in the case of a specific outburst of asteroidal activity, one needs to know, in the first step, whether the asteroid passed through a corridor of numerous meteoroid stream a short time before its activity occurred. Unfortunately, the compactness and numerosity of the streams in the interplanetary space (the main belt in our context) is unknown for a majority of the showers. We nevertheless predict the passages of a given asteroid through every known streams. An evaluation whether the stream can contain enough meteorids to collide with the asteroid should be additionally done by the researcher.

To help answering this question, we created a computer program that calculates the minimum orbit intersection distance (MOID) between the nominal orbit of a given object and the mean orbit of each known meteoroid stream. For

the close approaches of the orbits (a low MOID), the program gives their dates in a selected year. The description of the input data and program itself is given in the next section.

2. Description of program

2.1. Description of the code

The code consists of five executable files: "moid.exes", "relvel.exes", "basic-date.exes", "datelist.exes", and "arrange.exes". These files were compiled as the static binary files, therefore no compiler is needed to run them. They can be run, in the above-mentioned order, on any computer with a 64-bit processor. The corresponding source codes are also available on-line at https://www.astro.sk/caosp/Eedition/FullTexts/vol54no1/pp7-19.dat/. The basic norm was the Fortran 77.

In the UNIX/Linux operation system, the files can be run by using the single script named "calcdate.sh'. The speed of the calculation depends on the properties (mainly operation frequency) of the processor and selection of a specific asteroid (the number of the close approaches to the mean orbits of streams is different for various objects). However, the calculation does not typically exceed 15 seconds. The time of running of the first program, "moid.exes", is the longest one; the other programs need only a fraction of a second to be completed.

Before the running the code, the input must be prepared. The input and output data are described in the next two sub-sections.

2.2. Input data

2.2.1. Input data characterizing the investigated object

The characteristics of the object under interest should be edited by the user of the program into the input file named "object.dat". The object may not necessarily be a main-belt asteroid. However, its orbit must be elliptic and its eccentricity should be low (say $e < 0.5$). Otherwise the calculation of the MOID is not very precise for the approaches at a large value of true anomaly.

The following parameters should be inserted into the file "object.dat": the name of the object (15 characters in maximum), semi-major axis (in [au]), eccentricity [1], argument of perihelion [deg], longitude of ascending node [deg], inclination [deg], date (year-month-day) of the epoch the nominal orbit is referred to, mean anomaly of the object at the moment of epoch [deg], year of investigation of close approaches, and critical MOID [au], i.e. the upper value of MOID the user is interested in.

2.2.2. The known meteoroid streams

Currently, more than eight hundreds of meteoroid streams, which correspond to the meteor showers observed in the Earth's atmosphere, are known[1] (Jopek & Kaňuchová, 2014). We suppose that the known streams represent a majority of the streams crossing the region of the main asteroid belt. The provided program calculates the MOID of the orbits of an asteroid under the interest just with the mean orbits of these streams.

Because of the orbital similarity, the meteoroids of a given stream can approach a specific asteroid within a short arc of its orbit. The asteroid periodically passes this arc during a short time interval, with the period equal to its orbital period. The arc is situated around the point of the asteroid's orbit which is the nearest point to the mean orbit of the stream meteoroids. This is the reason why we think that the calculation of the MOID between the known, osculating orbit of the asteroid and the mean orbit of stream is useful. The points relevant to the MOID are specified by their true anomalies relevant to both orbits. The true anomaly of the asteroid can then be used to find the time when the asteroid passes the point of minimum approach to the mean orbit of a given stream.

In more detail, the mean orbits of the meteoroid streams in the List of All Showers of the Meteor Data Center (MDC) of the International Astronomical Union (IAU) are used as the default input related to the meteoroid streams; see the first footnote. In the list, the mean characteristics of some showers are given by two or more author teams. We call the set of parameters given by one author as a "solution" of the shower/stream. In total, the used list of meteoroid showers/streams contained 1305 solutions with a complete set of mean parameters. In calculations, all these solutions are taken into account. However, when we sum all the passages of an asteroid through a stream (Sect. 3) and this passage is predicted for more than a single solution, then the passage is regarded, of course, as a single event.

The input data-file with the meteoroid-stream orbits is named "allshowers.d". The data about one solution are in one line. The file contains, in the individual columns, the serial number of a solution, the official IAU number of a meteor shower, the identification number of solution (the solution can be identified with these two last numbers), mean parameters which are the solar longitude [deg], right ascension and declination of geocentric radiant [deg], geocentric velocity [km s^{-1}], semi-major axis [au], perihelion distance [au], eccentricity, argument of perihelion [deg], longitude of ascending node [deg], and inclination [deg]. In the last column, the number of meteors in the given solution is presented. This parameter can be useful in an estimate of the actual numerosity of the stream. If the number of meteors is large, i.e. the number density of

---

[1]The list of the known meteor showers can be found on the web pages of the Meteor Data Center of the International Astronomical Union: https://www.ta3.sk/IAUC22DB/MDC2022/Roje/roje_lista.php?corobic_roje=4&sort_roje=0 (as a default input file, we provide the list downloaded on August 19, 2022).

meteoroids is large in the part of the stream corridor crossing the Earth's orbit, then the overall number density of the stream can also be large. We note that a large number density of the stream can be expected when the number of meteors of the corresponding, Earth-observable meteor shower exceeds ~ 50, ~ 500, or ~ 2000 in the case of photographic, video, or radar observations of the shower, respectively.

On the other-hand, a low number of meteors do not necessarily indicate a low number density of the stream, because there can still be a larger number density in a part of the corridor situated farther from the Earth's orbit. In this case, information about the number density of meteoroids is not available, in fact. The default file "allshowers.d" can be completed, by the user, with the new solutions, which occur meanwhile.

2.3. Resultant data

2.3.1. Metadata

Each of the first four executable files produces an output file, which is the input into the next file. File "moid.exes" produces the data file named "moid.dw'. It contains the characteristics of the approaches within the critical MOID (selected by the user in the input file "object.dat"). If there is the sub-critical MOID for one, post-perihelion or pre-perihelion, arc of stream's orbit, then also the characteristics of the approach, regardless it is sub-critical or super-critical, for the other arc are given.

The characteristics of a given approach are written to five lines. The first line contains: the name of the object (a 15-character string in maximum), true anomalies of the object at the moment of its approach to the post-perihelion and pre-perihelion arcs of the stream orbit [deg], and the MOID for the post-perihelion and pre-perihelion arcs of the stream orbit [au].

The second line contains: the IAU number of the stream the object approached, the solution number of this stream, the number of meteors detected in the corresponding solution of a meteor shower, and true anomalies of the points in the post-perihelion and pre-perihelion arcs of the stream's mean orbit which are nearest to the object's orbit [deg]. The third line contains the mean orbital elements of the stream the object approached. These elements are given in order: perihelion distance [au], eccentricity [1], argument of perihelion [deg], longitude of ascending node [deg], and inclination to the ecliptic [deg].

The fourth (fifth) line contains the rectangular heliocentric ecliptical coordinates [au] of the asteroid and the stream meteoroid moving in the mean orbit of the stream at the moment of their closest approach on the post-perihelion (pre-periheion) arc of the meteoroid orbit.

Program "relvel.exes" produces its output data file named "relativeV.dw" with additional characteristics of the closest approaches. The characteristics of the given closest approach of the object to either post-perihelion or pre-

perihelion arc of the stream's mean orbit are given in four lines. The first line contains the name of the object (a 15-character string), true anomaly of the object at the moment of the closest approach [deg], MOID [au], the relative velocity between the object and the meteoroid moving in the mean orbit of the stream at the moment of the closest approach [km s^{-1}], and the angle between the heliocentric velocity vectors of the object and the meteoroid in the mean orbit at the moment of the closest approach [deg].

The characteristics in the second line are: the IAU number and solution number of the stream the object approached, the number of detected meteors in the corresponding solution of a meteor shower, and an indicator of the arc of the stream orbit to which the object approached (value 1 indicates the post-perihelion and value -1 the pre-perihelion arc).

In the third line of given characteristics, there are the rectangular heliocentric ecliptical coordinates [au] of the asteroid and the stream meteoroid moving in the mean orbit of the stream, both at the moment of the closest approach of both objects on the arc of meteoroid orbit specified in the 2nd line. The fourth line contains the rectangular components of the heliocentric ecliptical velocity vector [au day^{-1}] of the asteroid and components of an analogous vector of the stream meteoroid moving in the mean orbit of the stream, again at the moment of the closest approach of both objects on the arc of the meteoroid orbit specified in the 2nd line.

Program "basicdate.exes" produces the output data file "basicdate.dw". It contains further characteristics of the closest approach of the object to the post-perihelion and/or pre-perihelion arc of the mean orbit of a stream. The first of the two lines characterizing one approach contains: the name of the object (a 15 character string), the IAU number and solution number of the stream the object approached to, the number of detected meteors in the corresponding solution of a meteor shower, the true anomaly [deg] of the object at the moment of the closest approach, time of the closest approach [Julian date], orbital period of the object [day], indicator of the arc the object approached to (value 1 indicates the post-perihelion and value -1 the pre-perihelion arc), MOID [au], the mean orbital elements of the stream in order perihelion distance [au], eccentricity [1], argument of perihelion [deg], longitude of ascending node [deg], inclination [deg], relative velocity [km s^{-1}] between the object and meteoroid moving in the stream's mean orbit at the moment of the closest approach, and angle [deg] between the velocity vectors of the object and meteoroid in the mean orbit at the moment of the closest approach.

The second line of the approach characteristics in "basicdate.dw" contains the rectangular heliocentric ecliptical coordinates [au] of the asteroid at the moment of their closest approach, T_a, on the arc of the meteoroid orbit specified in the first line (columns 1$-$3), the rectangular components of the heliocentric ecliptical velocity vector [km s^{-1}] of the asteroid (columns 4$-$6) and the components of an analogous vector [km s^{-1}] of the stream meteoroid moving in the

mean orbit of the stream at the moment T_a on the arc of the meteoroid orbit specified in the first line (columns $7-9$).

Program "datelist.exes" finds out all close passages of the object through the meteoroid streams in the given year. This year is specified by the user in the input file "object.dat". The output is written into two files "unarranged????.d" and "unarr_vect????.d". Question marks in these names stand for the year of the investigation. The characteristics of each close approach (within the specified MOID) of the object to the mean orbit of the stream are provided in one line in each of both files. The individual columns in the output file "unarranged????.d" ("unarr_vect????.d") are the same as in the final output "datelist????.dat" ("vectors????.dat") − see the next sub-section.

2.3.2. List of predictions

As mentioned at the end of the previous sub-section, the final result is produced by the code "datelist.exes" and recorded to the output data files named "unarranged????.d" and "unarr_vect????.d". The last code named "arrange.exes" arranges the found close approaches in order of their increasing date. The final output data are stored in files "datelist????.dat" and "vectors????.dat". The characteristics of each approach are listed in one line in each file.

The columns of file "datelist????.dat" contain: the IAU number (IAUNo.) and solution number (Sol.) of the solution of a meteor shower, which corresponds to the stream the object approached to. Further, there is given the number of detected meteors of the shower (n). If $n = -1$, then the number of meteors is unknown. Then, the characteristics go on with the MOID [au] of the closest approach, heliocentric distance [au] of the meteoroid in the position of the closest approach (r_rel), relative velocity [km s^{-1}] (v_rel) between the object and meteoroid moving in the stream's mean orbit at the moment of the approach, angle [deg] between the velocity vectors of the object and meteoroid, and the date [year month day] of the closest approach.

File "vectors????.dat" contains the rectangular heliocentric ecliptical coordinates [au] of the asteroid at the moment of their closest approach, T_a, on the arc of the meteoroid orbit specified in the first line (in columns $1-3$), the rectangular components of the heliocentric ecliptical velocity vector [km s^{-1}] of the asteroid (columns $4-6$), and the components of an analogous vector [km s^{-1}] of the stream meteoroid moving in the mean orbit of the stream on the arc of the meteoroid orbit specified in the first line (columns $7-9$). Both vectors are given in time T_a.

The heliocentric velocity vector of the possible impactor can be expected not be the same as the heliocentric velocity vector of the meteoroid moving in the mean orbit, of course. Nevertheless, both impactor and hypothetical meteoroid in the mean orbit will obviously move in a similar orbit, therefore a rough match of both vectors can be expected. Thus, an eventual approximate agreement of the velocity vector of an impactor found in a simulation of the impact and that

of the meteoroid in the mean orbit is an indication supporting the hypothesis of an impactor from the specific stream.

3. Remark about the total approaches

Beside creating the program, we intended to clarify a wider context of the usage of the program. In this course, we estimated the total number of passages of all main-belt asteroids through all known meteoroid streams per year. To find this number, we considered the known asteroids with characteristics published on-line by the Minor Planet Center (MPC) of the IAU[2]. From the list of all asteroids, we selected those with a relatively reliable orbit, which had been determined on the basis of observations in, at least, three oppositions. We delimited the main belt by the perihelion distance larger than the aphelion distance of the orbit of Mars, $q > 1.666$ au, and by the aphelion distance smaller than the perihelion distance of Jupiter, $Q < 4.951$ au. The list of such asteroids contained 1,020,990 objects.

It appears that there is a huge number of close approaches of asteroids to the known meteoroid streams. For example, we performed the calculations for the approaches with a MOID lower than 0.05 au. The widths of stream corridors are unknown, therefore it is impossible to determine an average critical MOID. It seems that the width may exceed 0.15 au (the MOID of comet 1P/Halley, the parent body of the Orionids, from the Earth's orbit was found to be 0.155 au (Neslušan et al., 1998), therefore the width of the Orionid stream has to be larger than this MOID). However, some minor, diffuse showers can move in a narrower corridor. The value of 0.05 au may be regarded as a good compromise for a characteristic width of the stream.

For the critical MOID equal to 0.05 au, we found 23,202,210.5 passages of asteroids through the meteoroid streams a year. In more detail, this result is the average of passages in ten years, from 2023 to 2032. During this decade, the number varies from 22,981,394 to 23,348,851 and only 624 to 829 of 1,020,990 objects considered were found not to pass through any stream. In a year, the asteroid, that was found to cross the streams most frequently, passed the streams 109 times (asteroid 554211). The distribution of the number of passages in each of five years (2023−2027) is shown in Fig. 1. From this figure one can read that the largest number of meteors approached the mean orbit 11 to 12 times (in years 2023 and 2024, it was 11 times and in the other three years 12 times). We further found that the average number of approaches varied from 22.5 to 22.9. The median number was the same in these years; specifically, a half of all considered asteroids approached to the mean orbit of a stream more than 18 times per year.

It would be interesting to know an average probability that an inactive main-belt asteroid becomes active due to a meteoroid impact. Unfortunately, we do

---

[2]https://www.minorplanetcenter.net/iau/mpc.html (downloaded on August 3, 2022)
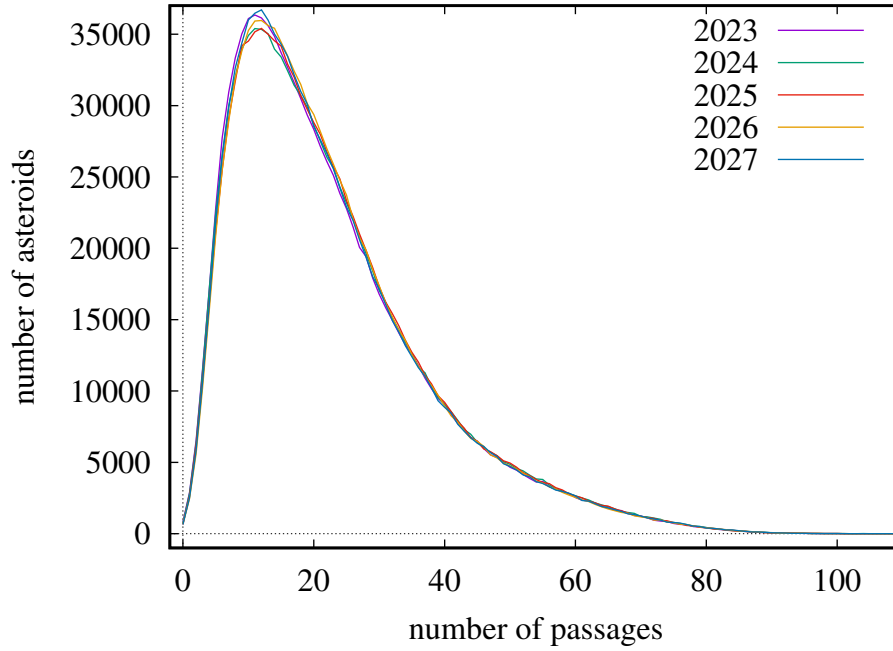
Figure 1. The distribution of the number of passages of asteroids through the known meteoroid stream within the distance of 0.05 au in a given year.

not have the sufficient input data to estimate such a probability. The width of the orbital corridor of meteoroid streams and the number density of meteoroids in the streams and sporadic background is unknown. The size-distributions of meteoroids is known only for several streams and only in the region around the Earth's orbit.

4. Some examples of possible triggering

There are several known asteroids, which were discovered to be inactive, but later a significant increase in brightness was observed. One may ask whether their outburst might have been triggered by an impact of a stream meteoroid. To answer this question, it is necessary to know, except of other, whether the asteroid passed through a stream or streams a certain period before the activity occurred. In this section, we provide such information about the passages of three asteroids, 493 Griseldis, 6478 Gault, and 62412 (2000 SY178), for the period starting two months before their outburst, or before their first outburst, and ending in time of their outburst, or the last observed outburst.

Table 1. The dates of the closest approaches of asteroids 493 Griseldis, 6478 Gault, and 62412 (2000 SY178) to the meteoroid streams in the period starting two months before their first observed outburst and ending in time of their last observed outburst. The listed parameters are: IAU - the official IAU number of shower, S. - the number of solution of the shower (some showers were reported by more than a single author team), n - number of meteors, arc - arc to which the asteroid approached, MOID - the minimum orbit intersection distance [au], r_{obj} - heliocentric distance of the asteroid [au], v_{rel} - its relative velocity in respect to a meteoroid moving in the mean orbit of the stream [km s^{-1}], and the angle between the velocity vectors of the asteroid and the meteoroid [deg], all at the moment of the closest approach of the asteroid to the mean orbit of the stream. The date of the closest approach is given in the last column.

IAU	S.	n	arc	MOID	r_{obj}	v_{rel}	angle	date
				493 Griseldis				
#0351	0	519	post-perih.	0.0111	2.36	28.30	107.28	2015 1 23.31
#0370	0	739	pre-perih.	0.0122	2.34	20.38	99.67	2015 1 29.31
#0354	0	823	post-perih.	0.0399	2.34	24.78	101.99	2015 1 29.31
#1115	0	7	post-perih.	0.0562	2.34	25.42	104.59	2015 1 31.31
#0165	2	89	pre-perih.	0.0857	2.33	21.94	100.14	2015 2 2.31
#1171	0	801	post-perih.	0.0272	2.29	28.56	113.85	2015 2 19.31
#0727	0	10	pre-perih.	0.0068	2.28	15.35	86.26	2015 2 22.31
#0513	0	77	pre-perih.	0.0598	2.27	16.05	84.84	2015 2 27.31
#0324	1	4	post-perih.	0.0614	2.26	25.23	97.45	2015 3 4.31
#1073	0	66	pre-perih.	0.0353	2.23	24.04	82.14	2015 3 14.31
#0428	1	22	pre-perih.	0.0614	2.22	16.17	85.83	2015 3 16.31
#0564	0	33	post-perih.	0.0446	2.22	28.96	97.41	2015 3 17.31
#0324	0	203	post-perih.	0.0416	2.22	25.98	97.76	2015 3 19.31
				6478 Gault				
#0219	1	17	pre-perih.	0.0547	2.13	15.39	45.88	2013 7 21.58
#0263	0	2	pre-perih.	0.0789	2.14	18.65	80.98	2013 7 22.58
#0219	0	5	pre-perih.	0.0983	2.14	22.98	60.64	2013 7 22.58
#0018	0	18	pre-perih.	0.0954	2.15	29.50	103.92	2013 7 27.58
#0094	1	2	post-perih.	0.0776	2.16	27.26	105.56	2013 8 2.58
#0714	0	7	pre-perih.	0.0431	2.16	13.52	33.88	2013 8 3.58
#0202	1	949	post-perih.	0.0506	2.18	35.10	104.14	2013 8 12.58
#0173	2		pre-perih.	0.0701	2.19	21.88	93.00	2013 8 16.58
#0289	0		pre-perih.	0.0436	2.21	21.67	91.57	2013 8 26.58
#0025	1	53	pre-perih.	0.0295	2.22	17.82	60.63	2013 8 31.58
#0173	3	288	pre-perih.	0.0559	2.23	21.27	93.30	2013 9 2.58
#0038	0	3	post-perih.	0.0636	2.24	40.35	148.90	2013 9 9.58
#0096	6	74	post-perih.	0.0653	2.25	24.95	102.53	2013 9 11.58
#1054	0	26	pre-perih.	0.0644	2.25	33.63	85.76	2013 9 12.58
#0017	2	22	pre-perih.	0.0516	2.26	17.10	62.07	2013 9 17.58
#0017	1	25	pre-perih.	0.0503	2.27	16.03	58.35	2013 9 19.58
#0631	0	57	pre-perih.	0.0630	2.27	16.04	60.33	2013 9 20.58

Table 1. Continued.

IAU	S.	n	arc	MOID	r_{obj}	v_{rel}	angle	date
#0096	2	7	post-perih.	0.0069	2.27	26.87	108.07	2013 9 21.58
#0449	0	7	post-perih.	0.0089	2.27	10.30	33.23	2013 9 21.58
				62412 SY178				
#1091	0	159	pre-perih.	0.0299	3.03	12.17	48.16	2014 2 1.18
#0232	0	2	pre-perih.	0.0077	3.04	8.05	47.25	2014 2 7.18
#0803	0	77	post-perih.	0.0608	3.05	14.66	87.40	2014 2 25.18
#0645	0	10	pre-perih.	0.0944	3.05	33.69	133.51	2014 2 28.18
#0199	0	6	post-perih.	0.0822	3.06	17.79	83.97	2014 3 18.18
#0069	0		pre-perih.	0.0808	3.07	15.16	90.79	2014 3 27.18
#0069	1	70	pre-perih.	0.0588	3.07	14.94	90.51	2014 4 2.18
#1132	0	1721	pre-perih.	0.0152	3.09	15.46	91.58	2014 4 22.18
#1042	0	16	post-perih.	0.0881	3.09	15.64	88.73	2014 4 27.18

The outburst of 493 Griseldis occurred on March 17−21, 2015 (Tholen et al., 2015). According to Chandler et al. (2019), 6478 Gault started its comet-like activity in 2013 and this activity persists until the present (the first outburst was detected on September 22, 2013). The mechanism of this long-term activity is probably something other than a meteoroid impact. The outburst of 62412 (2000 SY178) was detected, for the first time, on March 28, 2014 and lasted until May 2, 2014 (Sheppard & Trujillo, 2015).

The dates of the passages of these objects through some streams, before their first outburst, are listed in Table 1. The structure of this table is the same as the output from the computer program written into file "datelist????.dat". Specifically, we provide the dates for the closest approaches of a given asteroid within the MOID equal to 0.1 au. During the two-month period before the outburst, each of them passed through a few streams.

493 Griseldis crossed the corridors of the December σ-Virginids, #428 and 61-Ursae Majorids, #564 immediately before the outburst. As well it also crossed the ϵ-Perseids, #324 when its activity increased. Of these, the 61-Ursae Majorids and ϵ-Perseids are the established showers according to the MDC List of Established Showers. On February 19, 2015, the asteroid passed through quite a numerous shower − the January γ-Camelopardalids, #1171. In year 2015, this asteroid passed through 66 streams. It is significantly more than the average or median number of passages.

Immediately before the first outburst, 6478 Gault crossed the orbital corridors of the δ-Arietids, #631, the established shower Northern δ-Cancrids, #96, and April β-Sextantids, #449. The last shower was meanwhile removed from the Working List, therefore its existence is questionable. One to three days before the outburst, it also crossed the corridor of established Northern Taurids, #17, which are numerous, though the number of meteors of their solutions in Table 1

is not very large. The number of passages of the asteroid through the streams in 2013 was 70, which is also a much larger number than the average or median.

Asteroid 62412 (2000 SY178) crossed the established stream Southern μ-Sagittariids, #69, immediately before its first outburst. In this case, we can see an uncertainty of our calculation due to uncertain data on meteor streams. The closest approach on March 27, 2014 is predicted for the solution No. 0 of the shower. For solution No. 1, the closest approach is calculated to occur on April 2, 2014, i.e. 6 days later. During the 62412's activity, the object passed a relatively numerous stream of 3-Sagittariids, #1132, on April 22, 2014. However, the calculations resulted in only 21 passages of this asteroid through the meteoroid stream in 2014, which is comparable to the average.

We could see that several passages of the asteroids through the meteoroid streams occurred in all these randomly selected examples. In two cases, this number significantly exceeded the average (see the distribution of passages in Fig. 1). Nevertheless, further information would be needed if one wanted to evaluate the probability that the activity was triggered by a meteoroid impact.

5. Conclusion

We created a computer program to calculate the MOID between the orbit of a Solar-System small body and the known set of mean orbits of known meteoroid streams. When the MOID is low enough, then we can assume that the object passed or will pass through the orbital corridor of the stream. Such a passage or passages are the necessary condition to suspect that the activity could be triggered by an impact of a meteoroid, which is a member of the stream. The program, static-binary executable files as well as the source code, are public-domain and, therefore, available along with this article. It is also accessible on the GitHub service: https://github.com/neslusan/BELTCROSS2

The program can be especially useful to check if an asteroid, which was observed to become active, passed through a meteoroid stream, and through which stream, a short time before the beginning of the activity. The basic characteristics of the closest encounter of the asteroid with the stream are provided by the program.

References

Chandler, C. O., Kueny, J., Gustafsson, A., et al., Six Years of Sustained Activity in (6478) Gault. 2019, *Astrophysical Journal Letters*, **877**, L12, DOI: 10.3847/2041-8213/ab1aaa

Cunningham, L. E., Periodic Comet Wilson-Harrington (1949g). 1950, *IAU Circular*, **1250**, 3

Devogèle, M., Ferrais, M., Jehin, E., et al., (6478) Gault: physical characterization of an active main-belt asteroid. 2021, *Monthly Notices of the Royal Astronomical Society*, **505**, 245, DOI: 10.1093/mnras/stab1252

Drahus, M., Waniak, W., Tendulkar, S., et al., Fast Rotation and Trailing Fragments of the Active Asteroid P/2012 F5 (Gibbs). 2015, *Astrophysical Journal Letters*, **802**, L8, DOI: 10.1088/2041-8205/802/1/L8

Hsieh, H. H., Jewitt, D., Lacerda, P., Lowry, S. C., & Snodgrass, C., The return of activity in main-belt comet 133P/Elst-Pizarro. 2010, *Monthly Notices of the Royal Astronomical Society*, **403**, 363, DOI: 10.1111/j.1365-2966.2009.16120.x

Ivanova, O., Skorov, Y., Luk'yanyk, I., et al., Activity of (6478) Gault during 2019 January 13-March 28. 2020, *Monthly Notices of the Royal Astronomical Society*, **496**, 2636, DOI: 10.1093/mnras/staa1630

Jewitt, D., The Active Asteroids. 2012, *Astronomical Journal*, **143**, 66, DOI: 10.1088/0004-6256/143/3/66

Jewitt, D., Hsieh, H., & Agarwal, J., The Active Asteroids. 2015, in *Asteroids IV*, 221–241

Jopek, T. J. & Kaňuchová, Z., Current status of the IAU MDC Meteor Showers Database. 2014, in *Meteoroids 2013*, ed. T. J. Jopek, F. J. M. Rietmeijer, J. Watanabe, & I. P. Williams, 353–364

Kim, Y., Ishiguro, M., & Lee, M. G., New Observational Evidence of Active Asteroid P/2010 A2: Slow Rotation of the Largest Fragment. 2017a, *Astrophysical Journal, Letters*, **842**, L23, DOI: 10.3847/2041-8213/aa7944

Kim, Y., Ishiguro, M., Michikami, T., & Nakamura, A. M., Anisotropic Ejection from Active Asteroid P/2010 A2: An Implication of Impact Shattering on an Asteroid. 2017b, *Astronomical Journal*, **153**, 228, DOI: 10.3847/1538-3881/aa69bb

Kleyna, J. T., Hainaut, O. R., Meech, K. J., et al., The Sporadic Activity of (6478) Gault: A YORP-driven Event? 2019, *Astrophysical Journal Letters*, **874**, L20, DOI: 10.3847/2041-8213/ab0f40

Neslušan, L., Ivanova, O., Husárik, M., Svoren, J., & Seman Krišandová, Z., Dust productivity and impact collision of the asteroid (596) Scheila. 2016, *Planetary and Space Science*, **125**, 37, DOI: 10.1016/j.pss.2016.01.017

Neslušan, L., Svoreň, J., & Porubčan, V., A computer program for calculation of a theoretical meteor-stream radiant. 1998, *Astronomy and Astrophysics*, **331**, 411

Sheppard, S. S. & Trujillo, C., Discovery and Characteristics of the Rapidly Rotating Active Asteroid (62412) 2000 SY178 in the Main Belt. 2015, *Astronomical Journal*, **149**, 44, DOI: 10.1088/0004-6256/149/2/44

Tholen, D. J., Sheppard, S. S., & Trujillo, C. A., Evidence for an Impact Event on (493) Griseldis. 2015, in AAS/Division for Planetary Sciences Meeting Abstracts, Vol. **47**, *AAS/Division for Planetary Sciences Meeting Abstracts #47*, 414.03

Whipple, F. L., A Comet Model. II. Physical Relations for Comets and Meteors. 1951, *Astrophysical Journal*, **113**, 464, DOI: 10.1086/145416

Negative and positive superhumps of V503 Cyg as seen in TESS data. I. Seasons 2019 and 2021

E. Pavlenko[1], N. Pit[1] and T. Kato[2]

[1] *Crimean astrophysical observatory of RAS, Crimea (E-mail: eppavlenko@gmail.com)*

[2] *Department of Astronomy, Kyoto University, Kyoto 606-8502, Japan*

Abstract. We report the TESS observations of the SU UMa-type dwarf nova V503 Cyg in 2019 and 2021 during a superoutburst, normal outbursts and quiescence. We identified stage A of the growing superhumps and stage B in positive superhump evolution. We found that the stage A lasted $\sim$ 0.8 d; during stage B a mean period of 0.081367(93) d decreased with the derivative $P_{dot}/P = -4.8 * 10^{-5}$. We estimated the mass ratio $q = 0.195$ using a fractional period excess for stage B. The quiescent state was represented by a strong signal at negative superhumps and a weak one at the orbital period. We detected a gradual increase of the 0.076-d period of negative superhumps in quiescence preceding normal outbursts in 2019 and 2021, and an abrupt decrease of the period during normal outbursts. This means that the radius of the accretion disk increases sharply during the outburst and gradually decreases towards the onset of the next outburst. Such behavior is consistent with the thermal-tidal instability model.

We found that the light curve folded on the orbital period shows a profile that changes from double-peak to single-peak, respectively, in the tilted and non-tilted state of the accretion disk. We speculate that this difference may be caused by a state of the accretion disk: in the tilted disk state, one spot is the hot spot on the edge of the disk, while another one may be a spot caused by the matter hitting the inner disk. During the non-tilted disk state, there is one spot on its edge.

Key words: accretion, accretion disks – cataclysmic variables – stars: dwarf novae – stars: individual: V503 Cyg

1. Introduction

SU UMa type dwarf novae are a subtype of cataclysmic variables with orbital periods ranging from $\sim$ 76 minutes to 3 hours and a mass ratio of ≤ 0.25 (Warner, 1995; Whitehurst, 1988; Lubow, 1991). They exhibit two types of outbursts: "normal" outbursts, lasting 2-3 days, caused by the thermal instability of the accretion disk and "superoutbursts", lasting 10-20 days, caused by the thermal-tidal instability model (Osaki, 1989, 1996). Normal outbursts are more frequent events and are localized between superoutbursts. The disk matter accretes (but

not completely) onto the white dwarf during each normal outburst (for general information on cataclysmic variables and dwarf novae, see e.g. Warner (1995)), thus, by the beginning of the next outburst, the radius of the disk R_d is larger than at the beginning of the previous one, and eventually it reaches a 3:1 resonant radius $R_d < 0.47a$, where a is the binary separation at which a tidal instability is triggered and a superoutburst occurs. The disk begins to precess in the orbital plane (prograde apsidal precession). As a result of precession, so-called positive superhumps (the wave-like changes in brightness with varying amplitudes, up to several tenths of a magnitude) appear, the period P_{sh} of which is several percents larger than the orbital one. This period is related to the orbital period P_{orb} and the precession period P_{prec} by the relation

$$1/P_{prec} = 1/P_{orb} - 1/P_{sh}. \tag{1}$$

Period of positive superhumps systematically varies: it is constant and biggest during the superhumps growing (stage A), variable during the next stage B and shorter, stable at a late stage C (Kato et al., 2009).

Another type of accretion disk precession is the retrograde nodal precession, probably caused by an accretion disk tilted to the orbital plane (Montgomery & Martin, 2010; Wood et al., 2011). This precession results in negative superhumps with a period slightly shorter than the orbital one. While positive superhumps are an attribute of cataclysmic variables with a mass ratio ≤ 0.3, the negative superhumps can appear in systems with any mass ratio (Montgomery, 2010). However, there are far fewer known cataclysmic variables with negative superhumps than with positive ones.

V503 Cyg is an active dwarf nova of the SU UMa type (Harvey et al., 1995). Its orbital period obtained from both radial vilocity (Harvey et al., 1995) and photometry (Pavlenko et al., 2012) is 0.07776 d, the interval between superoutbursts (supercycle) is 89 d. The interval between adjacent normal outbursts (cycle) varied from 7 to 30 d on a scale of ~ 20 years. Negative superhumps with a period of 0.076 d were found by Harvey et al. (1995) and Szkody et al. (1989) in epoch of infrequent outbursts. Later a disappearance of negative superhumps was recorded by Pavlenko et al. (2012) along with a decrease in the normal cycle to 8-9 d. Yet in 2002 Kato et al. (2002) noticed a decrease in the normal cycle of V503 Cyg. This was an observational confirmation of the idea of Osaki & Kato (2013b) about the appearance/disappearance of negative superhumps with the lengthening/reduction of the normal cycle. Information about V503 Cyg state (with or without a disk tilt) and periodic processes for different years is presented in Table 1.

2. Observations

Observations of the V503 Cyg were carried out by the NASA Transiting Exoplanet Survey Satellite (TESS) during two seasons at 2-min cadence. The first

Table 1. V503 state and types of periodicity

Binary state	Cycle	Period	Reference
With disk tilt		Negative superhumps 0.0760 d	Szkody et al. (1989)
With disk tilt	30 d	Negative superhumps 0.075694 d	Harvey et al. (1995)
		Positive superhumps 0.081041 d	-"-
		Orbital 0.077708 d	-"-
Without disk tilt	7-9 d		Kato et al. (2002)
Without disk tilt	8-9 d	Orbital 0.077760 d	Pavlenko et al. (2012)
Without disk tilt		Orbital 0.0777591 d	Kato et al. (2014)
Without disk tilt		Positive superhumps 0.081446 d	-"-

season took place in 2019 between JD 2458683 and 2458737. The second season occured in 2021 between JD 2459420 and 2459446. The TESS band-pass is wide $\sim 600 - 1,000$ nm, see Ricker et al. (2015) for a description of TESS.

3. Results

3.1. V503 Cyg long-term light curves

The long-term light curve of V503 Cyg is presented in Fig. 1. It includes the
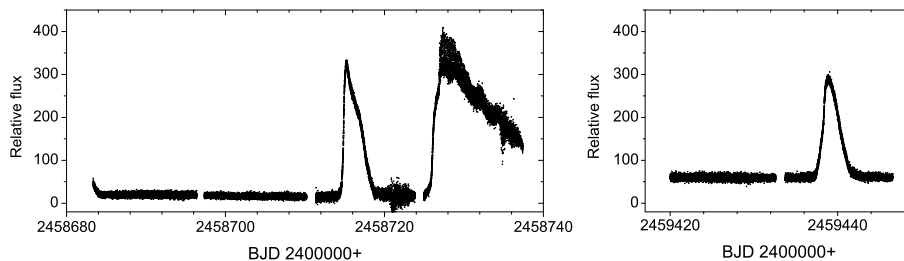
Figure 1. The overall light curve in 2019 (left) and 2021 (right). Data are expressed in relative flux.

superoutburst, a normal outburst, a quiescent state around and in between in 2019, a normal outburst and quiescent state around it in 2021. The total duration of both normal outbursts was about four days, but their profiles were different. The 2019 outburst has a sharper increase in brightness compared to decrease, so it is an "outside-in" type outburst, and the 2021 outburst is

rather an "inside-out" type one (Smak (1984)). According to the AAVSO data, a slight excess of brightness at the beginning of TESS 2019 set of observations corresponds to the end of the normal outburst. So one can conclude that the time between two normal outbursts (a normal cycle) was about 34 days which is comparable to the 30-day normal cycle recorded by Harvey et al. (1995) in the era of negative superhumps in the 1994 quiescence.

3.2. Periodicity in outbursts and quiescence

During all states of the V503 Cyg activity a short-term periodicity around 1.8 – 2 hours has been observed. Some examples of the light curves in the quiescence, the normal outburst and the superoutburst are shown in Fig. 2.
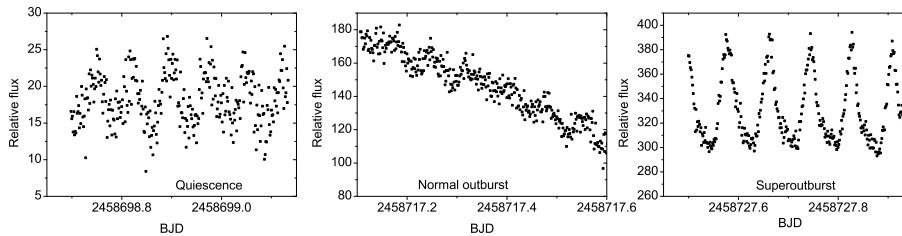

Figure 2. Examples of the light curves during the quiescence, the normal outburst and the superoutburst. Data are expressed in the relative flux.

As expected, the brightness changes in the quiescent state occurred with a different period than in the superoutburst. This is illustrated in Fig. 3, where there are the periodograms computed by the Stellingwerf method implemented in the ISDA package by Pel't (1980) for the quiescent state that preceded the 2019 normal outburst and for the 2019 superoutburst. It can be seen from the periodograms that an average period of brightness variations during the superoutburst was 0.081367(93) days, while in the quiescence it was 0.076063(12) days. These values are close to the periods of positive and negative superhumps, respectively, registered earlier (see Table 1). Broad peaks indicate that both periods have undergone changes over time. The continuity of observations provided by TESS made it possible to determine the frequencies of brightness changes in rather narrow time ranges; in this case, the duration of each range was 0.8 d, which ensured the accuracy of determining the period in the 4th decimal place. The result is presented in Fig. 4. The graphs show that the periods of both types of superhumps do change with time, but the nature of these changes is different. Let us consider the changes in positive and negative superhumps in more detail.

3.2.1. Evolution of positive superhumps and mass ratio

To identify the stages of the positive superhumps evolution for the 2019 super-outburst, we have determined the moments of maximum brightness of positive superhumps $MaxBJD$ and calculated the values of O-C using the ephemeris

$$MaxBJD = 2458726.51 + 0.08145 * E. \tag{2}$$

Fig. 5 shows the O-C values along with superhump amplitudes and the super-outburst light curve. The superoutburst started with a precursor in a form of a
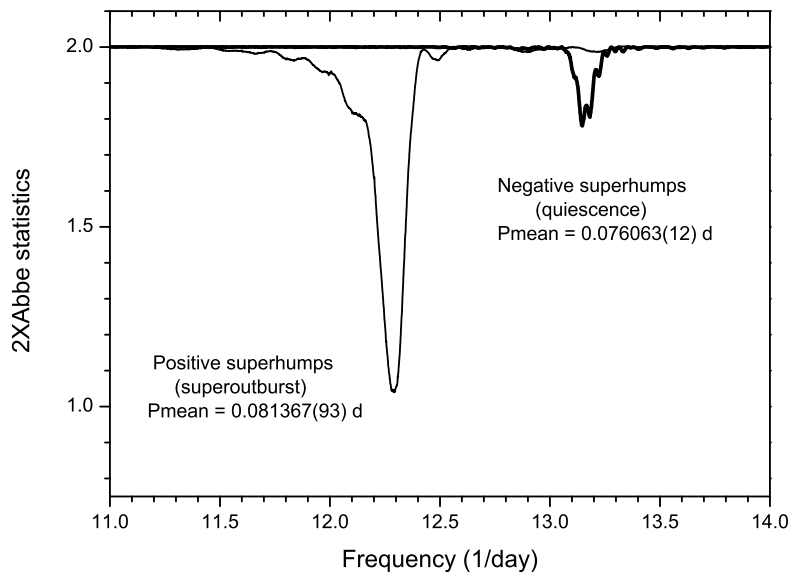

Figure 3. The periodograms for the superoutburst (thin line) and the 2019 quiescence (bold line). The peaks point to the mean period of positive superhumps in the super-outburst and negative superhumps in the quiescence that is limited by the normal outburst.

sharp brightness increase lasting a third of a day, followed by a slower brightening that lasted about 0.7 day and a sloping plateau with duration of at least 10 days (see Fig. 6). The precursor is thought as a normal outburst launching a superoutburst. As it can be seen in the bottom panel of Fig. 6, superhumps appeared already at the precursor stage. The fact that the superhumps appeared not at the main superoutburst, but at the precursor stage confirms the validity of a thermal-tidal instability theory (Osaki, 1996). From the beginning of the appearance of superhumps until they reached their maximum amplitude, only 10 cycles passed. We identified this interval as stage "A" (Kato et al.,
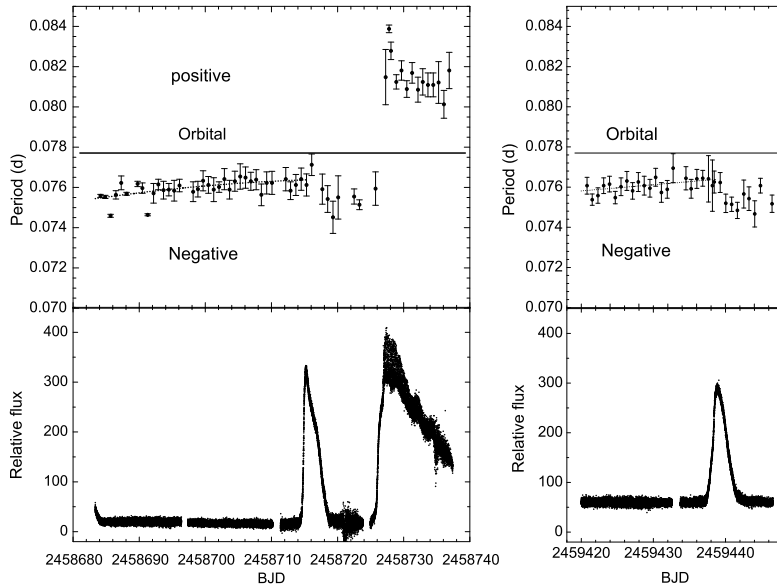
Figure 4. Upper panel: the period of negative superhumps in the quiescence and positive superhumps in the superoutburst. Lower panel: 2019 and 2021 light curves.

2009) of the positive superhumps growing and, approximating this O-C segment with a straight line, determined the period of superhumps to be equal to $P_A = 0.08247(51)$ d. For this period, we found a fractional period excess $\epsilon^* = 0.057$ (~ 0.8 d) using the relation proposed by Kato & Osaki (2013),

$$\epsilon^* = 1 - P_{orb}/P_A. \tag{3}$$

Having reached the maximum amplitude, the superhumps entered stage "B". During this stage, the amplitude of superhumps decreased, the period also decreased with a derivative of $P_{dot}/P = -4.8 * 10^{-5}$.

Note that the period at extremely short stage A may be distorted due to the influence of previous negative superhumps and the subsequent influence of positive superhumps at stage B. A situation, when for some reason the period at stage A is not correctly determined, was considered by Kato (2022). He proposed to use the empirical relation between the mass ratio at the resonant radius of 3:1 and ϵ at stage B:

$$\epsilon = (P_{sh} - P_{orb})/P_{orb}, \tag{4}$$

where P_{sh} is the mean period of positive superhumps at the stage B. In our case, the average period at the plateau stage (stage B) is 0.08137 d and the orbital period 0.0777591 d give $\epsilon = 0.046$ and q = 0.195 (from Table 4 in Kato (2022)).

Fig. 7 illustrates in detail how the positive superhumps evolved during the stage "B" for each interval of the inclined superoutburst plateau when
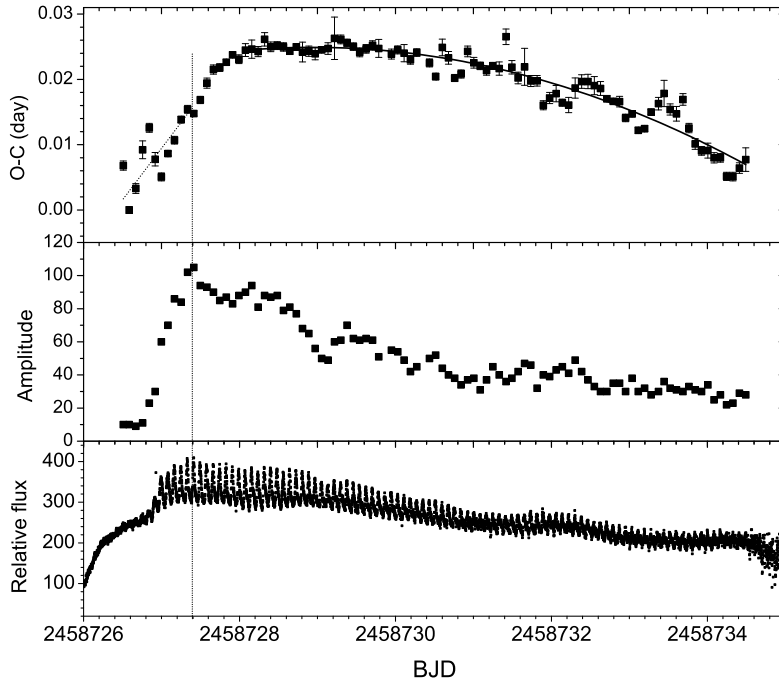
Figure 5. O-C of positive superhumps maxima (upper panel), their amplitudes (middle panel) and the superoutburst light curve shown in the top, middle and bottom panel respectively. The vertical line separates the stages "A" and "B" of the positive superhumps development.

it is divided into four intervals: BJD=2458727.08-2458728.95 (a), 2458729.27-2458730.73 (b), 2458731.33-2458732.93 (c) and 2458733.33-2558734 (d). Periodograms show the decrease of periods: the average values of the period are $P_a = 0.08211(18)$; $P_b = 0.08110(23)$; $P_c = 0.08126(21)$; $P_d = 0.08087(26)$ in these intervals. The corresponding phase curves show decrease of the amplitude and profile changes along the superoutburst plateau. As in earlier observations (Kato et al., 2014), the profile was a single peak at the beginning of the superoutburst and became a double peak one at the end of the superoutburst.

Next, we carried out the prewhitening procedure by subtracting the light variations corresponding to each interval with a period of positive superhumps. The periodograms constructed for the data residuals are shown in Fig. 8. The residual light variations in the first interval (a) are close to the orbital frequency F_{orb} and the beat period $2F^+ - F_{orb}$, where F^+ is the average frequency of positive superhumps in this interval. The second interval (c) does not contain any significant frequencies and the corresponding periodogram is not shown
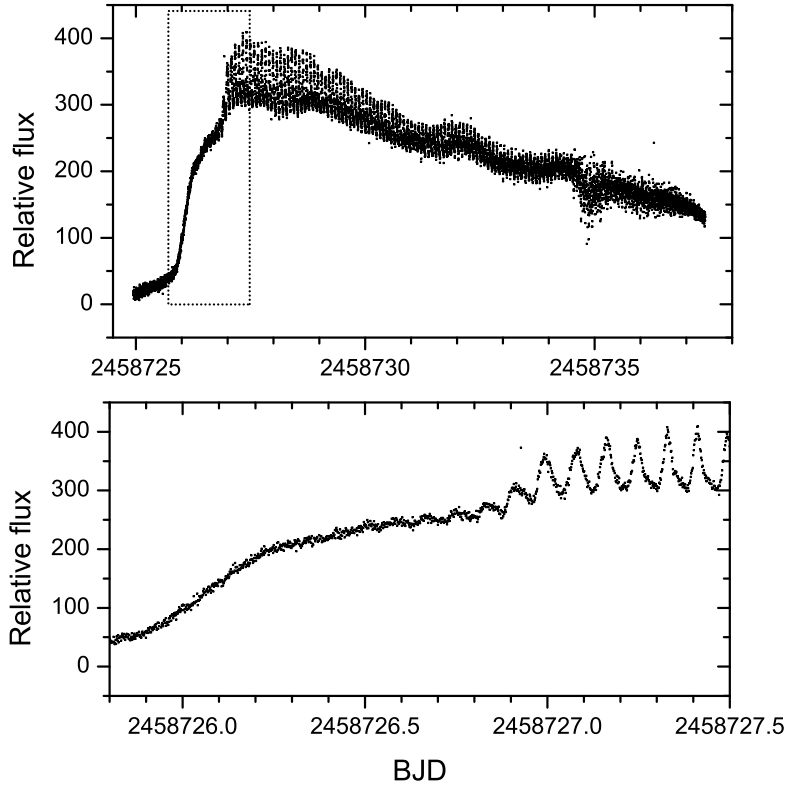
Figure 6. The superoutburst (upper panel). Its fragment, demonstrating the appearance and development of positive superhumps, is marked with a rectangle and shown in more detail in the bottom panel.

in the figure. Periodograms for the third (c) and fourth intervals (d) have a slight excess of the signal in the vicinity of the average frequency of negative superhumps. This may indicate that negative superhumps also exist during a supeoutburst, but they are hardly distinguishable against the background of the overwhelming power of positive superhumps.

3.2.2. Evolution of negative superhumps

As it was seen in Fig 4, negative superhumps between neighboring normal outbursts in 2019 (JD ∼2458684 – ∼2458711) show a gradual increase in the period (decrease in frequency). During the outburst, which began on JD 2458711, there is a sharp increase in frequency, which slowly decreases after the end of the outburst. The same behavior is observed for the 2021 outburst. The pattern of a
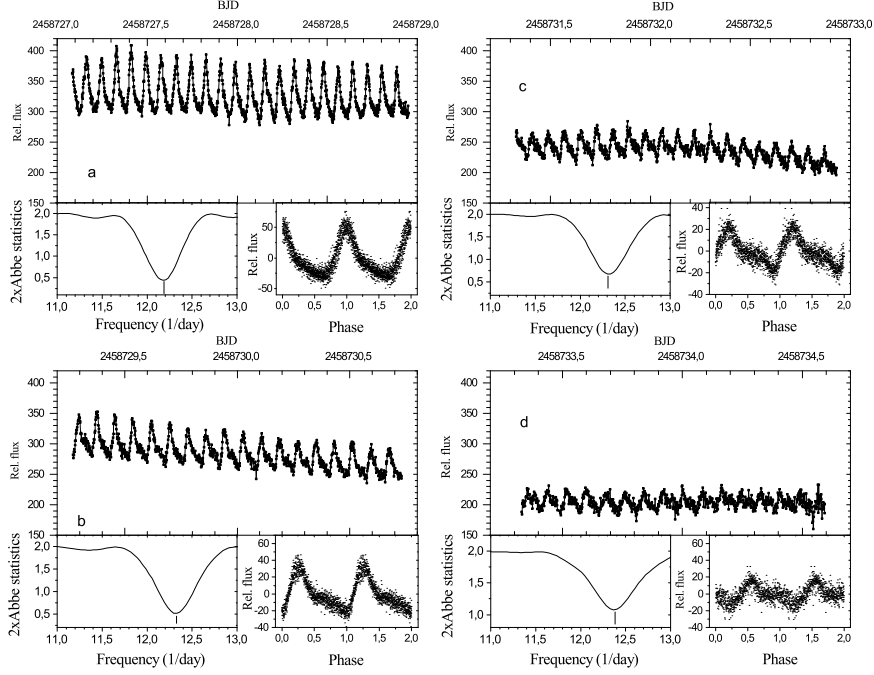
Figure 7. Original light curves, corresponding periodograms and phase light curves for different parts "a", "b", c" and "d" (see the explanations in the text) of the super-outburst plateau. The time of the first measurement in each interval was taken as the initial epoch, i.e. BJD 2458727.08448 for interval a, 2458729.27059 for b, 2458731.32892 for c and 2458733.33031 for d.

frequency change is similar to what Osaki and Kato found in the Kepler dwarf nova V1504 Cyg (Osaki & Kato, 2013b).

We also analyzed the period variation in both normal outbursts and their vicinity in more detail using the O-C method. In this case, for the brightness maxima of the negative superhumps for the first normal outburst, we used the ephemeris

$$MaxHJD = 2458711.398 + 0.07616 * E \tag{5}$$

and for the second - ephemeris

$$MaxHJD = 2459433.778 + 0.07616 * E. \tag{6}$$

The O-C course for both normal outbursts is shown in Fig.9. In both cases, at the maximum of each normal outburst, there was an abrupt decrease in the period (increase in frequency) of negative superhumps. After the end of each outburst, the period gradually increased during a normal cycle (see Fig. 4). A
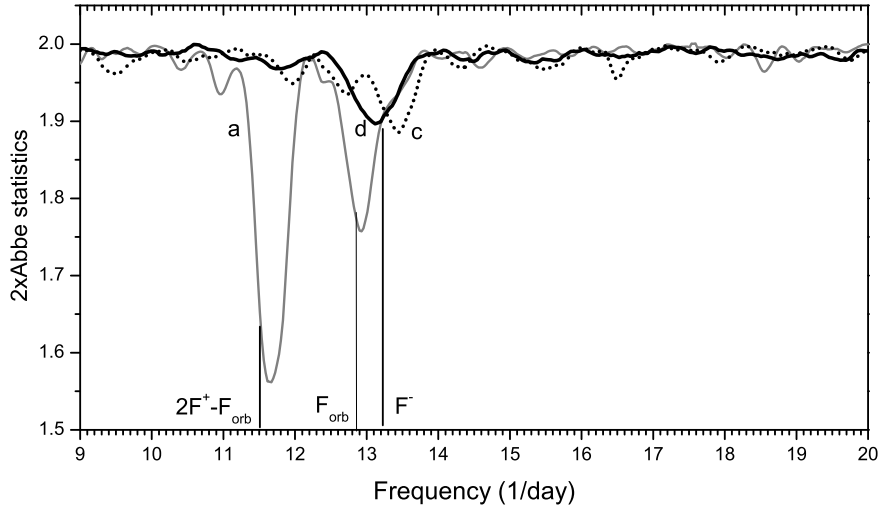
**Figure 8.** Periodograms for the prewhitened data at different parts "a", "c" and "d" of the superoutburst plateau. The position of the orbital frequency and combination of positive superhumps and orbital variations frequencies is marked by lines. The region of negative superhumps is shown by the grey streap.

similar behavior was first observed in the Kepler V1504 Cyg by Osaki & Kato (2013b).

3.2.3. Orbital modulation

Although there is no prominent evidence of the orbital period in the periodogram presented in Fig. 3, we decided to check this more carefully: to remove the mean negative superhump period from the all the quiescent TESS data and to analyse residuals. The resulting periodogram does contain a weak signal at the orbital period (Fig.11, left) that is hidden in the periodogram of Fig. 3. Note that this mean light curve profile ("orbital light curve") is a two-humped one, with humps separated by half a period. The amplitude of a larger hump is about $0^m.06$. However, the orbital profile in the epoch of the orbital period dominance and the absence of negative superhumps in the 2010 (Pavlenko et al., 2012) and 2011-2012 quiescence states without a disk tilt (Kato et al., 2013) (see Fig.11, right) is one-humped with an amplitude of $\sim 0^m.2$.

To see a potential change of the waveform of orbital variation during the quiescence, we calculated periodograms for several selected intervals of the 2019 and 2021 quiescence (see Fig. 12). One could see that while the larger hump is stable at all intervals, the smaller hump displays a slightly variable amplitude.
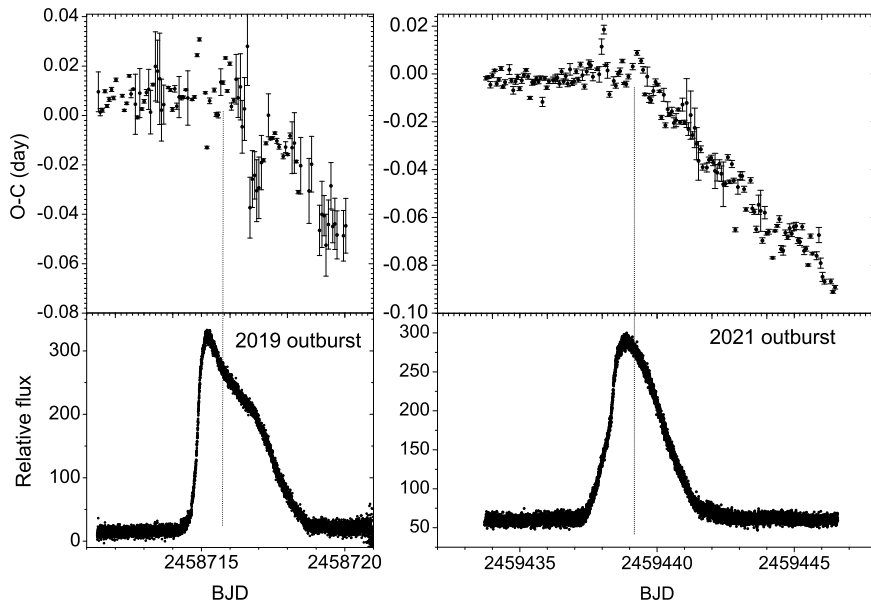
Figure 9. O-C of the negative superhumps maxima (top) and the corresponding light curves. The line is drawn through a sharp change in the O-C behavior.

4. Discussion

4.1. Accretion disk radius

According to Larwood (1998), the frequency of negative superhumps is related to the radius of the accretion disk by a simplified relation

$$\nu_{neg}/\nu_{orb} = 1 + \eta * 3/7(q/(1+q)^{1/2}) * (R_d/a)^{3/2} * cos\theta, \tag{7}$$

where ν_{neg} is the frequency of negative superhumps; ν_{orb} is the orbital frequency, q is the mass ratio, $cos\theta \sim 1$ for a small disk inclination angle, a is the binary separation, and η is a correction factor depending on the distribution of matter density in the disk. Reconciliation of this formula to the evolution of negative superhumps found by us shows that the radius of the accretion disk abruptly increases during the normal outburst and gradually decreases towards the onset of a next outburst. Similar phenomena were obtained for the Kepler V1504 Cyg (Osaki and Kato) and for the ground-based observations of MN Dra (Sklyanov et al., 2020), and NY Her (Pavlenko et al., 2021). Such behavior of the accretion disk is in accordance with the prediction of the thermal-tidal instability model.

As for the estimation of the disk radius, we have to know the correction factor η, which is unknown for the V503 Cyg in quiescence. Using equation (7) for q=0.195, $\nu_{orb} = 12.86$, the mean frequencies of negative superhumps ν_{neg}

$= 13.20(4)$ and $13.09(5)$; $\nu_{neg} = 13.20(4)$ and $13.09(4)$ at the start and the
end of the 2019 and 2021 quiescence, we calculated the dependence of the disk
radius on η (see Fig. 10). The range of probable disk radius values is limited
by the possible $\eta=1.94$-2.12 (Osaki & Kato, 2013a) and the 3:1 resonant radius
unattainable in a normal outburst. One could see that a larger η corresponds
to smaller radii. Despite of an unknown density distribution of matter in the
V503 Cyg disk, we can take $\eta = 1.22$ that Osaki & Kato (2013a) assumed for
the quiescent disk of the Kepler V1504 Cyg. In this case we obtain in average a
decrease of the disk radius from $0.43(3)a$ to $0.33(4)a$ during the quiescent state
between two normal outbursts (Fig. 10). Although these values may look close
to reality (see, for example, a discussion in Hellier (2001), we still cannot assert
their truth due to the unknown real density distribution of matter in the disk.
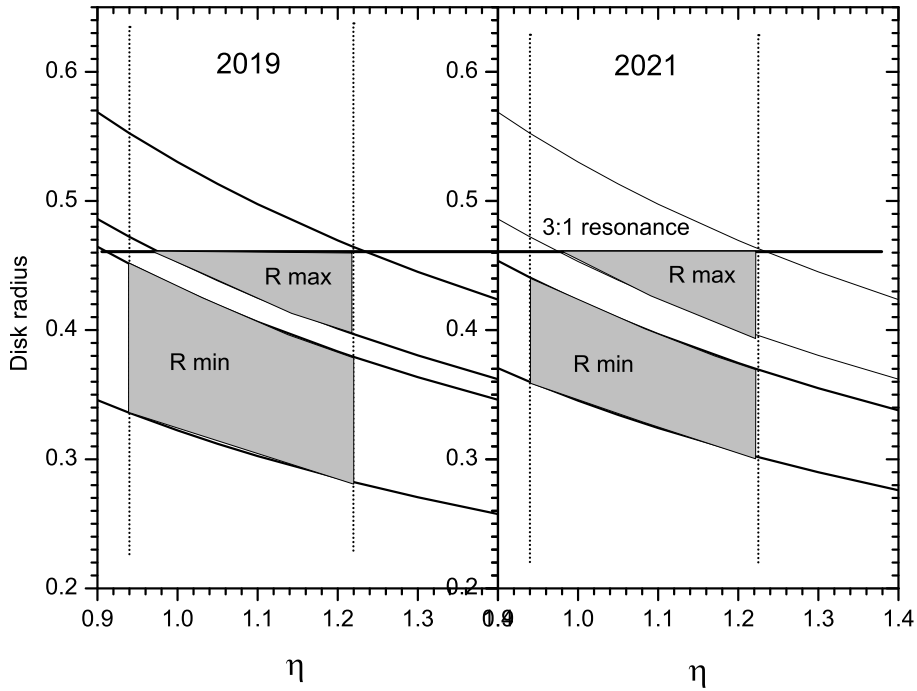
Figure 10. Dependence of the disk radius on a correction factor η for 2019 and 2021
years. The disk radius is expressed in the binary separation "a". The range of possible
radius values is shown in gray. The horizontal line corresponds to the 3:1 resonant
radius.
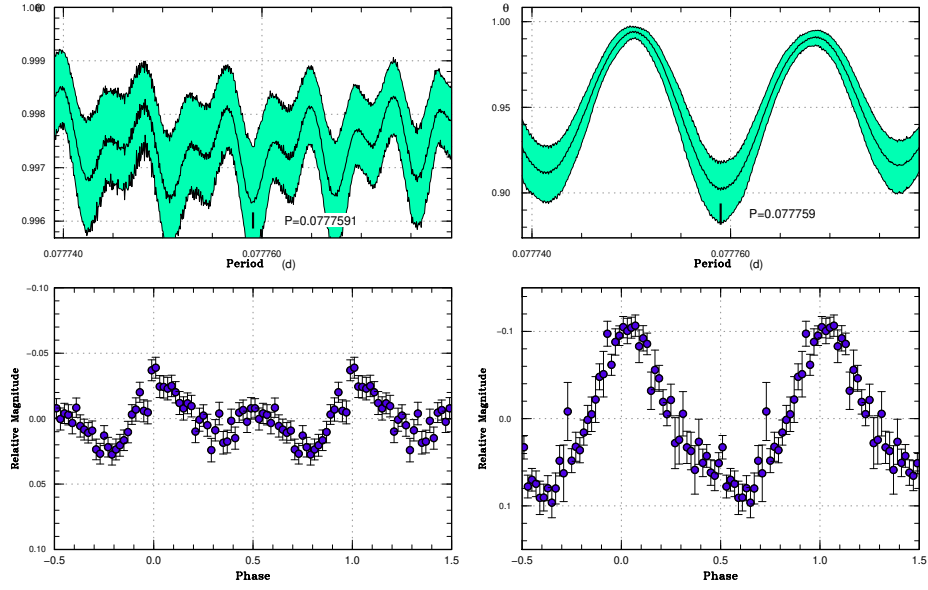
Figure 11. Orbital period. Periodograms and data folded on the orbital period for all the quiescent TESS data (left) and those for the 2011-2012 quiescence (right).
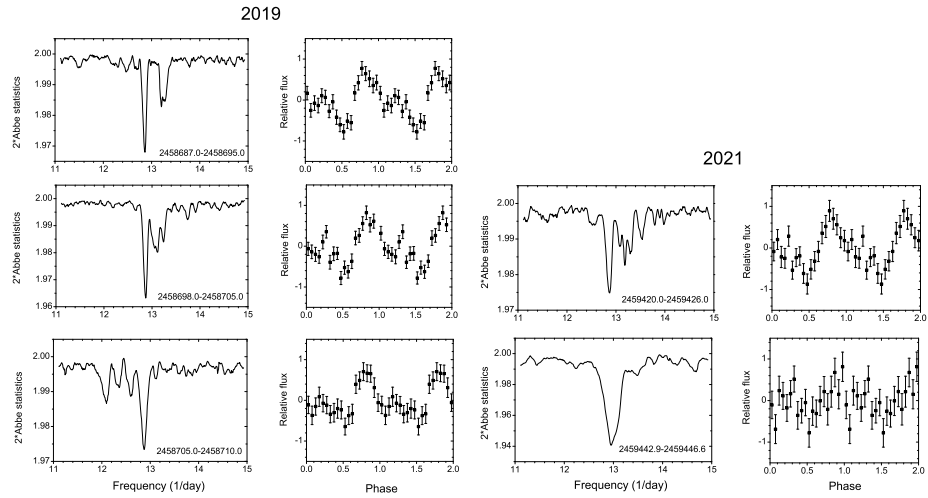
Figure 12. Orbital period. Periodograms and data folded on the orbital period for the selected quiescent TESS data in 2019 (left) and 2021 quiescence (right). The zero-epoch is 2458687.00118 and $Porb = 0.0777591$ d.

4.2. Difference of orbital light curve profile in tilted and non-tilted disk state

A potential contribution of various sources of radiation in CVs to the total radiation of the system may differ in different CVs, and this determines the waveform of orbital modulation. A "typical" profile of the light curve folded on the orbital period is one-humped due to a hot spot on the rim of the accretion disk. However, there are some exceptions. A one-humped light curve may be caused also by a reflection effect of the secondary component. Among cataclysmic variables there are cases of double-humped light curves with different interpretation. They may imply the contribution of ellipsoidality of a secondary, or a spiral structure of the accretion disk in the dwarf novae with a low mass ratio, predicted by Lin & Papaloizou (1979). Dai et al. (2018) suggested that double-humped orbital modulation in the systems with low inclination may be caused by two spots – one on the edge of disk, the other on its surface.

We believe that the change in the V503 Cyg orbital light curve profile is due to a change in the state of the accretion disk. As Kimura et al. (2020) noted, that contrary to the typical case of a non-tilted disk, in binaries with a tilted disk, the accretion stream not only hits the outer rim of the disk, but also reaches the inner part of the disk. The two-humped orbital profile of the TESS data may be due to the fact that in the state with a disk tilt, one spot appears to be the hot spot on the edge of disk, while another may be from a spot caused by the matter hitting an inner disk. During the state without a disk tilt, there is one spot on the edge of disk.

5. Conclusion

We analysed the photometric data of the SU UMa-type dwarf nova V503 Cyg obtained in 2019 and 2021 with the Transiting Exoplanet Survey Satellite (TESS). The main results are summarized as follows:

- The A and B stages in the positive superhumps evolution during the 2019 superoutburst were identified and the mass ratio was estimated.

- In 2019 and 2021 the strong negative superhumps dominanted during the quiescence and normal outbursts, so the binary state of V503 Cyg was with an accretion disk tilt. The period of negative superhumps showed cyclical changes: it increased slowly between normal outbursts and decreased sharply during the outburst. This reflects cyclic changes in the radius of the disk, consistent with the thermal-tidal instability model.

- It was found that in the 2019 quiet state a weak signal was detected at the orbital period. Its profile was double-humped, as opposed to the single-humped one observed in the era when the orbital signal was dominant. We hypothesized that the difference in profiles could be due to the different state of the binary system. The one-humped profile is caused by a hot spot on the edge of the non-

titled disk, and the two-humped one is associated with one spot on the edge of a tilted disk, and the second spot - in its inner part.

References

Dai, Z., Szkody, P., Kennedy, M., et al., A Phenomenological Model for the Light Curve of Three Quiescent Low-inclination Dwarf Novae and One Pre-cataclysmic Variable. 2018, *Astronomical Journal*, **156**, 153, DOI: 10.3847/1538-3881/aadb99

Harvey, D., Skillman, D. R., Patterson, J., & Ringwald, F. A., Superhumps in Cataclysmic Binaries. V. V503 Cygni. 1995, *Publications of the ASP*, **107**, 551, DOI: 10.1086/133591

Hellier, C. 2001, *Cataclysmic Variable Stars*

Kato, T., Evolution of short-period cataclysmic variables: implications from eclipse modeling and stage A superhump method (with New Year's gift). 2022, *arXiv e-prints*, arXiv:2201.02945, DOI: 10.48550/arXiv.2201.02945

Kato, T., Hambsch, F.-J., Maehara, H., et al., Survey of Period Variations of Superhumps in SU UMa-Type Dwarf Novae. IV. The Fourth Year (2011-2012). 2013, *Publications of the ASJ*, **65**, 23, DOI: 10.1093/pasj/65.1.23

Kato, T., Hambsch, F.-J., Maehara, H., et al., Survey of period variations of superhumps in SU UMa-type dwarf novae. V. The fifth year (2012-2013). 2014, *Publications of the ASJ*, **66**, 30, DOI: 10.1093/pasj/psu014

Kato, T., Imada, A., Uemura, M., et al., Survey of Period Variations of Superhumps in SU UMa-Type Dwarf Novae. 2009, *Publications of the ASJ*, **61**, S395, DOI: 10.1093/pasj/61.sp2.S395

Kato, T., Ishioka, R., & Uemura, M., Dramatic Changes in the Outburst Properties in V503 Cygni. 2002, *Publications of the ASJ*, **54**, 1029, DOI: 10.1093/pasj/54.6.1029

Kato, T. & Osaki, Y., New Method of Estimating Binary's Mass Ratios by Using Superhumps. 2013, *Publications of the ASJ*, **65**, 115, DOI: 10.1093/pasj/65.6.115

Kimura, M., Osaki, Y., Kato, T., & Mineshige, S., Thermal-viscous instability in tilted accretion disks: A possible application to IW Andromeda-type dwarf novae. 2020, *Publications of the ASJ*, **72**, 22, DOI: 10.1093/pasj/psz144

Larwood, J., On the precession of accretion discs in X-ray binaries. 1998, *Monthly Notices of the RAS*, **299**, L32, DOI: 10.1046/j.1365-8711.1998.01978.x

Lin, D. N. C. & Papaloizou, J., Tidal torques on accretion discs in binary systems with extreme mass ratios. 1979, *Monthly Notices of the RAS*, **186**, 799, DOI: 10.1093/mnras/186.4.799

Lubow, S. H., A Model for Tidally Driven Eccentric Instabilities in Fluid Disks. 1991, *Astrophysical Journal*, **381**, 259, DOI: 10.1086/170647

Montgomery, M., Earth, Moon, Sun, Accretion Disks, And Retrograde Precession. 2010, in American Astronomical Society Meeting Abstracts, Vol. **215**, *American Astronomical Society Meeting Abstracts #215*, 301.07

Montgomery, M. M. & Martin, E. L., A Common Source of Accretion Disk Tilt. 2010, *Astrophysical Journal*, **722**, 989, DOI: 10.1088/0004-637X/722/2/989

Osaki, Y., A model for the superoutburst phenomenon of SU Ursae MAjoris stars. 1989, *Publications of the ASJ*, **41**, 1005

Osaki, Y., Dwarf-Nova Outbursts. 1996, *Publications of the ASP*, **108**, 39, DOI: 10.1086/133689

Osaki, Y. & Kato, T., Study of Superoutbursts and Superhumps in SU UMa Stars by the Kepler Light Curves of V344 Lyrae and V1504 Cygni. 2013a, *Publications of the ASJ*, **65**, 95, DOI: 10.1093/pasj/65.5.95

Osaki, Y. & Kato, T., The Cause of the Superoutburst in SU UMa Stars is Finally Revealed by Kepler Light Curve of V1504 Cygni. 2013b, *Publications of the ASJ*, **65**, 50, DOI: 10.1093/pasj/65.3.50

Pavlenko, E. P., Samsonov, D. A., Antonyuk, O. I., et al., Photometry of the dwarf nova V503 Cyg in 2010. Orbital and other periods. 2012, *Astrophysics*, **55**, 494, DOI: 10.1007/s10511-012-9255-4

Pavlenko, E. P., Sosnovskii, A. A., Antonyuk, K. A., et al., Changes in the Period of Negative Superhumps of Type SU UMa Dwarf Novae. II. NY Her (2017 and 2020). 2021, *Astrophysics*, **64**, 293, DOI: 10.1007/s10511-021-09690-3

Pel't, Y. 1980, *Frequency analysis of astronomical time series.*

Ricker, G. R., Winn, J. N., Vanderspek, R., et al., Transiting Exoplanet Survey Satellite (TESS). 2015, *Journal of Astronomical Telescopes, Instruments, and Systems*, **1**, 014003, DOI: 10.1117/1.JATIS.1.1.014003

Sklyanov, A. S., Pavlenko, E. P., Antonyuk, K. A., et al., Variations in the Period of Negative Superhumps in SU UMa-Type Dwarf Novae. I. Mn Dra (2012-2017). 2020, *Astrophysics*, **63**, 200, DOI: 10.1007/s10511-020-09626-3

Smak, J., Accretion in cataclysmic binaries. IV. Accretion disks in dwarf novae. 1984, *Acta Astronomica*, **34**, 161

Szkody, P., Howell, S. B., Mateo, M., & Kreidl, T. J., CCD Time-Resolved Photometry of Faint Cataclysmic Variables. II. 1989, *Publications of the ASP*, **101**, 899, DOI: 10.1086/132550

Warner, B., Books-Received - Royal Observatory - Cape of Good Hope - 1820-1831 - the Founding of a Colonial Observatory. 1995, *Science*, **270**, 1859

Whitehurst, R., Numerical simulations of accretion discs - I. Superhumps : a tidal phenomenon of accretion discs. 1988, *Monthly Notices of the RAS*, **232**, 35, DOI: 10.1093/mnras/232.1.35

Wood, M. A., Still, M. D., Howell, S. B., Cannizzo, J. K., & Smale, A. P., V344 Lyrae: A Touchstone SU UMa Cataclysmic Variable in the Kepler Field. 2011, *Astrophysical Journal*, **741**, 105, DOI: 10.1088/0004-637X/741/2/105

The calculation of normal stars structure within the generalized polytropic model

M. Vavrukh[ID] **and D. Dzikovskyi**[ID]

Department of Astrophysics, Ivan Franko National University, Kyrylo &
Methodiy str. 8, 79005 Lviv, Ukraine (E-mail: mvavrukh@gmail.com)

Abstract. The generalized polytropic equation of state $P(\mathbf{r}) = K\big(\rho(\mathbf{r})/f(\mathbf{r})\big)^{4/3}$ for calculation of stars' characteristics of an arbitrary age with a spatially heterogeneous distribution of chemical composition ($f(\mathbf{r}) = \mu(\mathbf{r})/\bar{\mu}$, where $\mu(\mathbf{r})$ is the local value of the dimensionless molecular weight, and $\bar{\mu}$ is its average value over the star volume) was constructed by the Eddington method. Using the example of the Sun, it is shown that the standard polytropic model ($f(\mathbf{r}) = 1$) corresponds to the stars of zero age. The characteristics of the Sun in the modern epoch and their evolutionary changes were calculated. The obtained results are close to those based on the system of Schwarzschild equations. The proposed approach is applied to the calculation of the internal structure of the star model with axial rotation.

Key words: methods: analytical – stars: fundamental parameters – stars: interiors – stars: evolution

1. Introduction

Axial rotation of stars is an attribute of their existence. Traditionally, the influence of axial rotation on stars' characteristics is taken into account within the perturbation theory. Herewith, the zero approximation is a well-known polytropic model with spatially homogeneous chemical composition and equation of state $P(\mathbf{r}) = K[\rho(\mathbf{r})]^{1+1/n}$, where n and K are constants. In the particular case $n = 3$, this model was substantiated by Eddington at the beginning of the last century, when there was no information about the energy sources of stars and changes of chemical composition with the age of a star. The polytropic models with $n \neq 3$ have a phenomenological character. The theory of rotational polytropes was developed by Milne (1923), Chandrasekhar (1933), James (1964) and other researchers in the first half of the last century within the mechanical equilibrium equation. In the first of the two named works, the influence of rotation was taken into account as a perturbation and analytical expansions were used with accuracy to the square of angular velocity. The work of James (1964) is based on the numerical integration of the equilibrium equation.

The second stage in the development of the internal structure of stars, initiated in the middle of the last century, was based on the system of equations (Schwarzschild, 1958). However, in the study of solar structure and the evolution of stars with different masses (Eddington, 1988), there were employed spherically symmetrical models and rotation considered as a secondary factor. At the same time, Monaghan & Roxburgh (1965), Caimmi (1980), and Williams (1988) improved the semi-analytical theory of rotational polytropes with a spatially uniform chemical composition, corresponding to stars of zero age.

Already in the XXI-th century, a new direction of research has been arisen – the calculation of the internal structure of specific stars with high angular velocity. In particular, Kong et al. (2015) and Knopik et al. (2017), who focus on the internal structure of the star α Eri with angular velocity $\omega \approx 3 \cdot 10^{-5} \mathrm{s}^{-1}$, employed the computer 3D integration. However, the standard polytropic equation of state with index $n = 1$ reduces the persuasiveness of the obtained results for a star that is at the final stage of its evolution. The strict approach to the calculation of the internal structure of a star should be based on a system of differential equations. As it is known, the system of Schwarzschild equations for the model with a spherically symmetry consist of four ordinary differential equations. Taking into account the rotation leads to eight differential equations, which greatly complicated calculations. We propose a different approach to the calculation of characteristics of stars of different age at the presence of rotation. We find an approximate semi-analytical solutions of the mechanical equilibrium equation with rotation within a generalized equation of state, that allows us to take into account the spatially heterogeneous chemical composition, which arose as a result of thermonuclear reactions and corresponds to the star of certain age. Undoubtedly, such approach has a qualitative nature, but it greatly simplifies the calculations and plays the role of some express analysis for the selection of objects for the purpose of more detailed research.

In Section 2 there is substantiated the generalized polytropic model according to the Eddington method. The characteristics of the current Sun were calculated in Section 3 using the polytropic model with a spatially heterogeneous chemical composition. There were shown the advantages of such model compared with the standard model with $n = 3$. In the same section, there were calculated the evolutionary changes of the Sun's characteristics based on the modeling of the radial distribution of partial density of hydrogen. Section 4 is devoted to the influence of axial rotation on the characteristics of a star model, which is similar to the Sun, but has significant axial rotation.

2. The generalized equation of state

Using the Eddington method, we consider a model with spatially heterogeneous distribution of chemical composition, taking into account both gas and light pressure at the same time,

$$P_{\text{gas}}(\mathbf{r}) = \frac{k_B}{m_u \mu(\mathbf{r})}\, \rho(\mathbf{r})\, T(\mathbf{r}), \quad P_{\text{ph}}(\mathbf{r}) = \frac{a}{4}\, T^4(\mathbf{r}), \tag{1}$$

where $\rho(\mathbf{r})$ is the local density, $T(\mathbf{r})$ is the temperature, $\mu(\mathbf{r})$ is the local value of dimensionless (in atomic mass units m_u) molecular weight, $a = k_B^4 (\hbar c)^{-3} \pi^2 / 15$, k_B is the Boltzmann constant, c is the speed of light. According to the main Eddington assumption

$$P_{\text{gas}}(\mathbf{r}) = \beta P(\mathbf{r}), \quad P_{\text{ph}}(\mathbf{r}) = (1 - \beta) P(\mathbf{r}), \tag{2}$$

where $P(\mathbf{r})$ is the total pressure, and β is the constant independent on coordinates. By excluding the temperature from the system of equations (1) and (2), we obtain a relation between pressure and density in the form

$$P(\mathbf{r}) = K \left[\frac{\rho(\mathbf{r})}{f(\mathbf{r})} \right]^{4/3}, \quad f(\mathbf{r}) = \frac{\mu(\mathbf{r})}{\bar{\mu}}, \tag{3}$$

where $\bar{\mu}$ is the dimensionless parameter that represents the average value of the molecular weight by the volume of the star. Herewith,

$$K = \left\{ \frac{1 - \beta}{\beta^4} \cdot \frac{3}{a} \left(\frac{k_B}{m_u \bar{\mu}} \right)^4 \right\}^{1/3} \tag{4}$$

coincides with the value of the constant in the Eddington model, namely in the approximation $\mu(\mathbf{r}) = \bar{\mu}$, or $f(\mathbf{r}) = 1$, that corresponds to the star of zero age on the main sequence. Using the example of the Sun, we will show that the equation of state (3) better describes the internal structure of the star compared to the standard polytropic model. This applies not only to the characteristics of the Sun in the current epoch, but also to their evolutionary changes.

3. The internal structure of the Sun within the generalized polytropic model

Taking into account a small angular velocity of the Sun ($\approx 3 \cdot 10^{-6} \text{s}^{-1}$), we consider a spherically symmetrical model that corresponds to works performed on the system of Schwarzschild equations. We examine the mechanical equilibrium equation

$$\nabla P(r) = -\rho(r) \nabla \Phi_{\text{grav}}(r), \tag{5}$$

in which

$$\Phi_{\text{grav}}(r) = -G \int \frac{\rho(r^{'})d\mathbf{r}^{'}}{|\mathbf{r} - \mathbf{r}'|} \tag{6}$$

is the gravitational potential on the sphere of radius r. Using expression (3) and taking into account that

$$\left[\frac{\rho(r)}{f(r)}\right]^{-2/3} \nabla \left(\frac{\rho(r)}{f(r)}\right) = 3\nabla \left(\frac{\rho(r)}{f(r)}\right)^{1/3}, \tag{7}$$

equation (5) takes the form

$$4K\nabla^2 \left(\frac{\rho(r)}{f(r)}\right)^{1/3} = -f(r)\nabla^2\Phi_{\text{grav}}(r) - (\nabla f(r), \nabla\Phi_{\text{grav}}(r)). \tag{8}$$

In the spherically symmetrical model of a star with radius R

$$\Phi_{\text{grav}}(r) = -\frac{GM(r)}{r} - 4\pi G \int\limits_{r}^{R} \rho(r')r'dr', \tag{9}$$

where

$$M(r) = 4\pi \int\limits_{0}^{r} \rho(r^{'})(r^{'})^2 dr^{'} \tag{10}$$

is the mass of matter in the sphere of radius r, and $d\Phi_{\text{grav}}(r)/dr = GM(r)/r^2$. According to the Poisson equation $\Delta\Phi_{\text{grav}}(r) = 4\pi G\rho(r)$. Taking into account relation (9) and the next ones, we transform equation (8) to the integro-differential equation

$$4K\Delta \left(\frac{\rho(r)}{f(r)}\right)^{1/3} = -4\pi G\rho(r)f(r) - \frac{GM(r)}{r^2} \cdot \frac{df(r)}{dr}. \tag{11}$$

For a known function of $f(r)$, the solution of equation (11) determines the radial distribution of density $\rho(r)$. For a star of zero age $f(r) = 1$, equation (11) reduces to the differential equation for the standard polytropic model. For the convenience of integrating equation (11), let's introduce the dimensionless variables

$$\xi = r/\lambda, \quad y(\xi) = \left\{\frac{\rho(r)}{f(r)} \left[\frac{f_c}{\rho_c}\right]\right\}^{1/3}, \tag{12}$$

where λ is the scale of length, $\rho_c \equiv \rho(0)$, and $f_c \equiv f(0)$. Functions $\mu(r)$ and $f(r)$ are represented in the form

$$\mu(r) \equiv \mu(r/R) = \mu(\xi/\xi_1), \quad f(r) \equiv f(r/R) \equiv \frac{\mu(\xi/\xi_1)}{\bar{\mu}} =$$
$$= \frac{\mu(\xi/\xi_1)}{\mu(0)} \frac{\mu(0)}{\bar{\mu}} = f_c \frac{\mu(\xi/\xi_1)}{\mu(0)}, \tag{13}$$
$$\frac{df(r)}{dr} = \frac{df(r/R)}{Rd(r/R)} = \frac{df(\xi/\xi_1)}{\lambda\xi_1 d(\xi/\xi_1)},$$

where $\xi_1 = R/\lambda$ is the dimensionless value of the star radius. Let's take into account that

$$\Delta = r^{-2}\frac{d}{dr}\left(r^2\frac{d}{dr}\right) = \frac{1}{\lambda^2}\Delta_\xi, \ \ \Delta_\xi = \xi^{-2}\frac{d}{d\xi}\left(\xi^2\frac{d}{d\xi}\right),$$

let's multiply equation (11) by f_c/ρ_c and determine λ by

$$K = \pi G\left[\frac{\rho_c}{f_c}\right]^{2/3}\lambda^2. \tag{14}$$

As a result, we obtain the dimensionless form of the equilibrium equation

$$\Delta_\xi y(\xi) = -y^3(\xi)f^2(\xi/\xi_1) - \frac{f_c}{\xi_1}\cdot\frac{df(\xi/\xi_1)}{d(\xi/\xi_1)}\cdot\frac{1}{\xi^2}\int_0^\xi (\xi')^2 y^3(\xi')\,\frac{\mu(\xi'/\xi_1)}{\mu(0)}d\xi'. \tag{15}$$

According to the definition of the function $y(\xi)$, the regular solution of equation (15) must satisfy the boundary conditions

$$y(0) = 1, \quad \frac{dy}{d\xi} = 0 \ \text{ at } \ \xi = 0. \tag{16}$$

The dimensionless radius of the star ξ_1 is the root of equation $y(\xi) = 0$. Since ξ_1 plays the role of a parameter in equation (15), it is determined in a self-consistent way using the method of successive approximation during the numerical integration of this equation for a given function $f(\xi/\xi_1)$.

The function $y(\xi)$ and the dimensionless radius ξ_1 allow us to determine the unknown parameters of the problem λ, ρ_c and K from the system of equations

$$R_\odot = \lambda\,\xi_1, \quad M_\odot = 4\pi\lambda^3\rho_c\,\alpha, \quad K = \pi G\lambda^2\left(\frac{\rho_c}{f_c}\right)^{2/3} \tag{17}$$

with the known values of mass and radius of the Sun, where

$$\alpha = \int_0^{\xi_1}\xi^2 y^3(\xi)\frac{f(\xi/\xi_1)}{f(0)}d\xi = \int_0^{\xi_1}\xi^2 y^3(\xi)\frac{\mu(\xi/\xi_1)}{\mu(0)}d\xi. \tag{18}$$

3.1. The Sun characteristics within the standard polytropic model

The solution of the dimensionless equilibrium equation in the standard polytropic model ($f(r) = 1$) for $n = 3$ is well known and shown by curve 1 in Fig. 1. Herewith

$$\xi_1 = 6.89685\ldots, \quad \alpha = 2.01824\ldots. \tag{19}$$
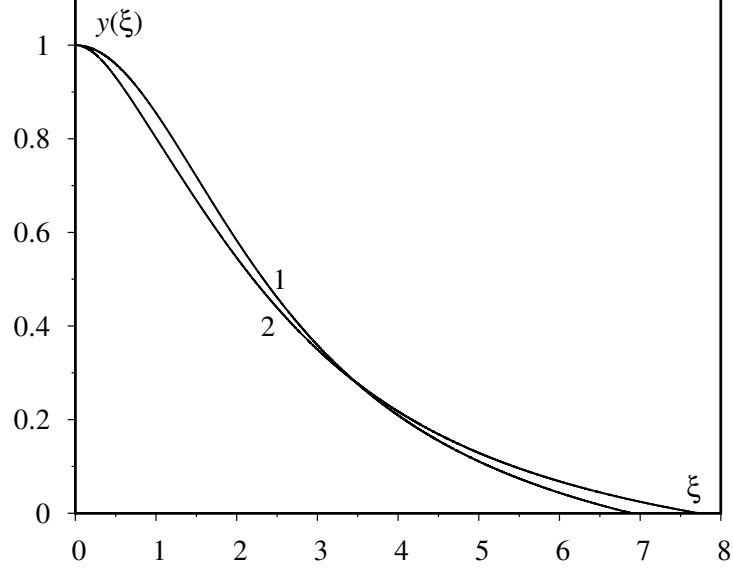
Figure 1. The solutions of the equilibrium equation. Curve 1 corresponds to the standard polytropic model, curve 2 – to the generalized model.

Using the observed values of the mass and radius of modern Sun ($M_\odot = 1.9891\ldots \cdot 10^{33}$g, $R_\odot = 6.9634\ldots \cdot 10^{10}$cm), we can determine the values of the parameters in the standard model

$$\lambda = 1.0098 \cdot 10^{10} \text{ cm}, \quad \rho_c = 76.1731 \text{ g cm}^{-3},$$
$$K = 3.8416 \cdot 10^{14} \text{ cm}^3 \text{ g}^{-1/3} \text{ s}^{-2}. \tag{20}$$

The radial density distribution in such approximation is determined by the expression

$$\rho(r) = \rho_c y_3^3\left(\frac{r}{\lambda}\right) = \rho_c y_3^3(x\xi_1), \tag{21}$$

where $x \equiv r/R_\odot$, and $y_3(\xi)$ is Emden's function for the polytropic index $n = 3$. The obtained value of the central density is close to that found by Sears (1964) for the Sun of zero age through the numerical integration of the system of Schwarzschild equations ($\rho_c = 90$ g cm^{-3}). If we use the value $R_\odot = 6.6460 \cdot 10^{10}$ cm (calculated by Sears (1964) for the zero age) instead of the modern radius of the Sun, then we obtain the specified values of the parameters

$$\lambda = 0.9571 \cdot 10^{10} \text{ cm}, \quad \rho_c = 87.6100 \text{ g cm}^{-3},$$
$$K = 3.8416 \cdot 10^{14} \text{ cm}^3 \text{ g}^{-1/3} \text{ s}^{-2}. \tag{22}$$

Such value of the central density coincides with the value obtained by Sears (1964) for the Sun of zero age. This indicates that the standard model with $n = 3$ is entirely applicable to the Sun at zero age, where the spatial distribution of chemical elements is uniform and corresponds to the Eddington approximation. But such model is not applicable for the modern Sun, where the central density is close to the value $\rho_c = 158 \text{ g cm}^{-3}$ (Sears, 1964).

3.2. The characteristics calculation in the generalized model of modern Sun

We use Emden's function for $n = 3$ as the zero approximation to find the solution of equation (15) by the iterative method. The coordinate dependence of the characteristics of the modern Sun was calculated through the numerical integration of the system of Schwarzschild equations by Sears (1964). Our aim is to compare the results of characteristic calculations for the modern Sun within the generalized model with those obtained by Sears (1964). For this, we use the coordinate dependence of the dimensionless molecular weight $\mu(r) \equiv \mu(r/R_\odot) = \mu(x)$, which was calculated by Lamers & Levesque (2017) for the values of the partial densities outside the core $X = 0.708$, $Y = 0.272$ and $Z = 0.020$. As shown in Fig. 2, the agreement is well-established almost everywhere in the interval $0 \leq x \leq 1$ (except for the surface layers) with the known expression

$$\mu(r/R_\odot) = \left\{ 2X(r/R_\odot) + \frac{3}{4}\, Y(r/R_\odot) + \frac{1}{2}\, Z(r/R_\odot) \right\}^{-1}, \qquad (23)$$

which corresponds to the total ionization of matter. To simplify calculations, we do not take into account the change of $\mu(r/R_\odot)$ in the surface region, extrapolating instead the molecular weight value in the intermediate region to the surface region. We represent the function $\mu(x)$ in the form of a Padé approximant,

$$\mu(x) = \left\{ \sum_{j=0}^{3} b_j\, x^j \right\}^{-1} \sum_{i=0}^{3} a_i\, x^i,$$
$$a_0 = 0.0149173,\ a_1 = -0.0868327,\ a_2 = 0.730856,\ a_3 = 1.7342,$$
$$b_0 = 0.0172646,\ b_1 = -0.0893741,\ b_2 = 1.0339,\ b_3 = 2.96529. \qquad (24)$$

Calculating $\bar{\mu}$ as the average value of $\mu(r/R_\odot)$ over the star volume,

$$\bar{\mu} = 3R_\odot^{-3} \int\limits_0^{R_\odot} \mu(r/R_\odot) r^2 dr = 3 \int\limits_0^1 x^2 \mu(x) dx, \qquad (25)$$

we represented in the analytical form the function $f(x) = \mu(x)/\bar{\mu}$, derivative df/dx, and $f(x)f_c^{-1} = \mu(x)/\mu(0)$. In Fig. 2 it is also shown the function $f(x)$ and
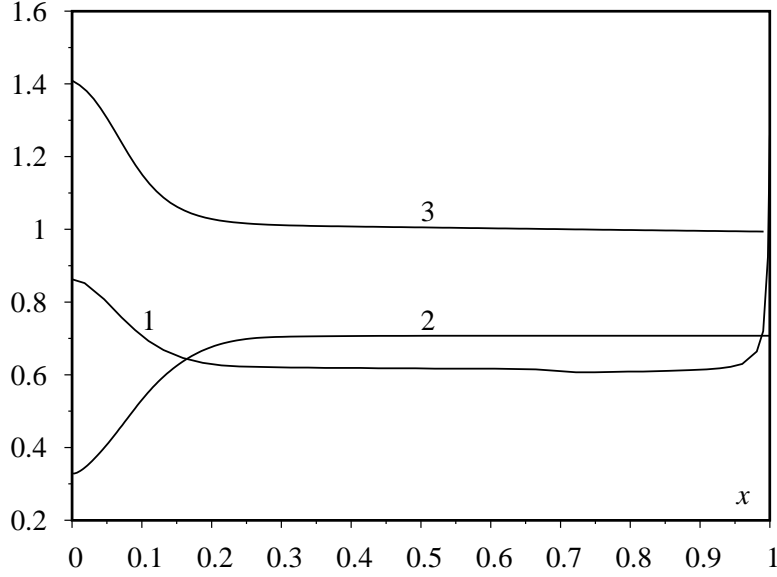
Figure 2. The coordinate dependence of the dimensionless molecular weight $\mu(x)$ (curve 1), the partial density of hydrogen $X(x)$ (curve 2) from Sears (1964) and Lamers & Levesque (2017), and the function $f(x)$ (curve 3).

the partial density of hydrogen $X(x)$ according to formula (23) and condition $X(x) + Y(x) + Z(x) = 1$. In order to analyze equation (15), we note that for a star with the age of the Sun, where thermonuclear reactions occur during $4.5 \cdot 10^9$ years, the molecular weight $\mu(r/R_\odot)$ in the core region is greater than the average value of $\bar{\mu}(f(r/R_0) > 1)$, and outside the core $\mu(r/R_\odot) \approx \bar{\mu}$, $(f(r) \approx 1)$. The nature of the solution to equation (15) is primarily determined by the first term on the right-hand side, while the second term (which is positive) plays the role of correction. Therefore, in the core region the condition $y(\xi) < y_3(\xi)$ must be satisfied, while outside the core the condition $y(\xi) > y_3(\xi)$ must be fulfilled. From there it follows that the dimensionless radius of the Sun ξ_1 in the generalized model must be greater than the value $\xi_1 = 6.89685\ldots$ of the standard model. The solution of equation (15) according to approximation (24) (curve 2) and the function $y_3(\xi)$ (curve 1) are shown in Fig. 1. In accordance with expressions (17) and (18) at $\xi_1 = 7.72441$ and $\alpha = 1.30993$, we have

$$
\begin{aligned}
&\lambda = 0.9015 \cdot 10^{10} \text{ cm}, \quad \rho_c = 164.9420 \text{ g cm}^{-3}, \\
&K = 4.0776 \cdot 10^{14} \text{ cm}^3 \text{ g}^{-1/3} \text{ s}^{-2}.
\end{aligned}
\tag{26}
$$
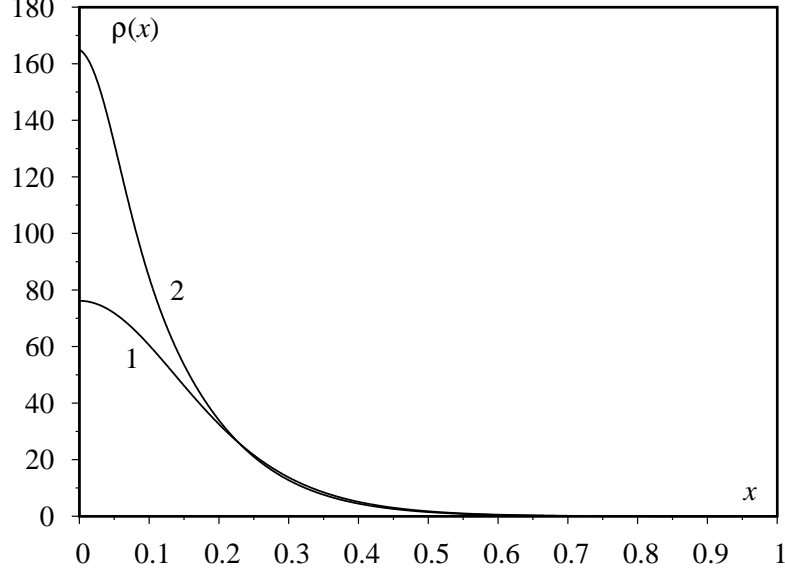
Figure 3. The distribution of density along the radius in different approximations. Curve 1 corresponds to the standard model, curve 2 – to the generalized model.

The density of matter is determined by the solution of equation (15),

$$\rho(r/R_\odot) = \rho(\xi/\xi_1) = \rho_c \frac{f(\xi/\xi_1)}{f_c} y^3(\xi). \tag{27}$$

In Fig. 3 the radial dependence of density compares in two models: curve 1 corresponds to the standard model, and curve 2 – to the generalized model. The radial dependence of density in the generalized model of the Sun, along with analogous values from Lamers & Levesque (2017), is shown in Fig. 4. The criterion for calculation is not only the central density but also other characteristics, including the gravitational and total energy of the star, moment of inertia, and the age of the star. To evaluate the age of the Sun, let's determine the hydrogen mass in the modern epoch

$$M_H = 4\pi \rho_c \lambda^3 \int\limits_0^{\xi_1} \xi^2 y^3(\xi) X(\xi/\xi_1) \frac{\mu(\xi/\xi_1)}{\mu(0)} d\xi = M_\odot \frac{\gamma}{\alpha}, \tag{28}$$

where α is determined by formula (18), and

$$\gamma = \int\limits_0^{\xi_1} \xi^2 y^3(\xi) X(\xi/\xi_1) \frac{\mu(\xi/\xi_1)}{\mu(0)} d\xi. \tag{29}$$
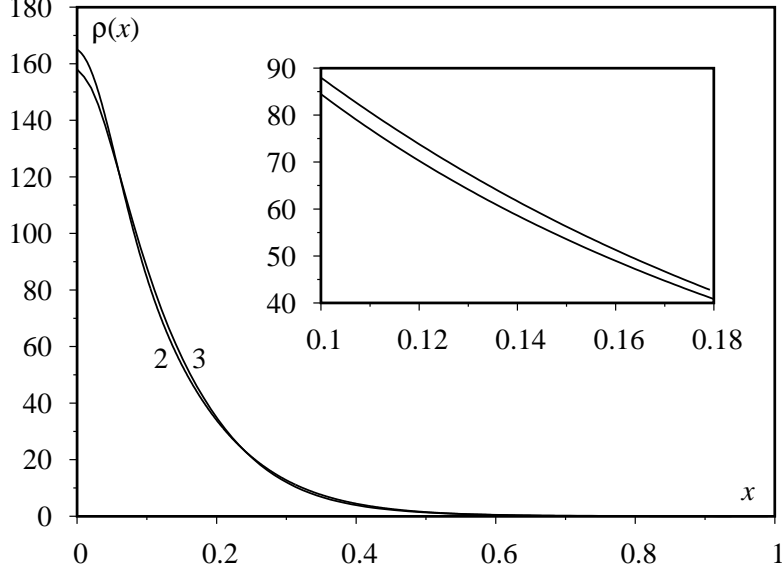
Figure 4. The distribution of density along the radius. Curve 2 corresponds to formula (15), curve 3 is taken from Lamers & Levesque (2017).

Since at the zero age phase $M_H = 0.708 \cdot M_\odot$, the loss of partial hydrogen mass is equal

$$\Delta M_H = \left(0.708 - \frac{\gamma}{\alpha}\right) M_\odot, \tag{30}$$

that corresponds to the mass defect $\delta_H = 0.00716 \cdot \Delta M_H$ and the radiation energy $\delta_H \cdot c^2$. Taking into account that the Sun's luminosity $L_\odot$ has changed only slightly during its existence, we can determine its age

$$t = \frac{\Delta M_H \cdot 0.00716 \cdot c^2}{L_\odot} = \frac{M_\odot}{L_\odot} \left(0.708 - \frac{\gamma}{\alpha}\right) 0.00716 \cdot c^2, \tag{31}$$

where $L_\odot$ is the Sun luminosity, c is the speed of light. For the modern Sun, $\gamma = 0.870$ and $\alpha = 1.310$, from which it follows that $t \approx 4.6 \cdot 10^9$ years. This value deviates from the generally accepted value by 2%. According to relations (17) and (27), the potential model energy is represented in the form

$$W = -\frac{1}{2}G \iint\limits_{V} \rho(r_1)\rho(r_2)|\mathbf{r}_1 - \mathbf{r}_2|^{-1}d\mathbf{r}_1 d\mathbf{r}_2 = -G\,\frac{M_\odot^2}{R_\odot}w,$$

$$w = \frac{\xi_1}{\alpha^2} \int\limits_0^{\xi_1} \xi\, y^3(\xi)\, \frac{\mu(\xi/\xi_1)}{\mu(0)}d\xi \int\limits_0^{\xi} \xi_2^2 y^3(\xi_2)\frac{\mu(\xi_2/\xi_1)}{\mu(0)}d\xi_2. \tag{32}$$

For the modern Sun $w \cong 1.656$. Using the result of the calculation $\rho(r/R_\odot)$ from Lamers & Levesque (2017), we obtain the analogous expressions

$$W_s = -G \, \frac{M_\odot^2}{R_\odot} w_s,$$

$$w_s = \frac{1}{\alpha_s^2} \int\limits_0^1 x\tilde{\rho}(x)dx \int\limits_0^x z^2 \tilde{\rho}(z)dz; \tag{33}$$

$$\alpha_s = \int\limits_0^1 x^2 \, \tilde{\rho}(x) \, dx; \quad \tilde{\rho} = \rho(x)/\rho_c.$$

As known from the polytropic theory, the volume density of internal energy

$$\mathcal{E}(\mathbf{r}) = 3P(\mathbf{r}) \tag{34}$$

for $n = 3$. In the case of a generalized polytrope

$$\mathcal{E}(\mathbf{r}) = 3K \left(\frac{\rho(\mathbf{r})}{f(\mathbf{r})} \right)^{4/3}, \tag{35}$$

therefore, the total internal energy

$$U = \int\limits_V \mathcal{E}(\mathbf{r})d\mathbf{r} = G \, \frac{M_\odot^2}{R_\odot} \, v,$$

$$v = 0.75 \, \xi_1 \, (\alpha \, f_c)^{-2} \int\limits_0^{\xi_1} \xi^2 y^4(\xi) \, d\xi \cong 1.655. \tag{36}$$

As in the standard polytropic theory, in the generalized model gravitational energy and internal energy are mutually compensated. In connection with the redistribution of matter with age along the radius, it is worth comparing the moment of inertia relative to the Sun's diameter both in the standard and generalized models. In the generalized model

$$I = \int\limits_V r^2 \, \sin^2 \theta \, \rho(r) \, d\mathbf{r} = M_\odot R_\odot^2 \cdot 2\beta \, (3\alpha \, \xi_1^2)^{-1}, \tag{37}$$

where

$$\beta = \int\limits_0^{\xi_1} \xi^4 \, y^3(\xi) \, \frac{\mu(\xi/\xi_1)}{\mu(0)} \, d\xi. \tag{38}$$

For the modern Sun $I \cong 6.485 \cdot 10^{53}$ g·cm^2. To obtain the moment of inertia of the Sun of zero age, we should use $\alpha = 2.018$, and replace the multiplier $\mu(\xi/\xi_1)/\mu(0)$

with a unit. This yields the value $I(t = 0) \cong 6.622 \cdot 10^{53}$ g $\cdot$ cm^2. Although the Sun's radius increases with the age, its moment of inertia decreases, leading to an increase in rotational velocity.

3.3. Evolutionary changes of the Sun characteristics

Comparing the characteristics of the Sun at zero age with its modern characteristics reveals an interesting problem in calculating their age dependence. For this purpose, we modeled the partial radial dependence of hydrogen in the Sun's core using curves that are shown in Fig. 5. The dotted straight line 1 corresponds to
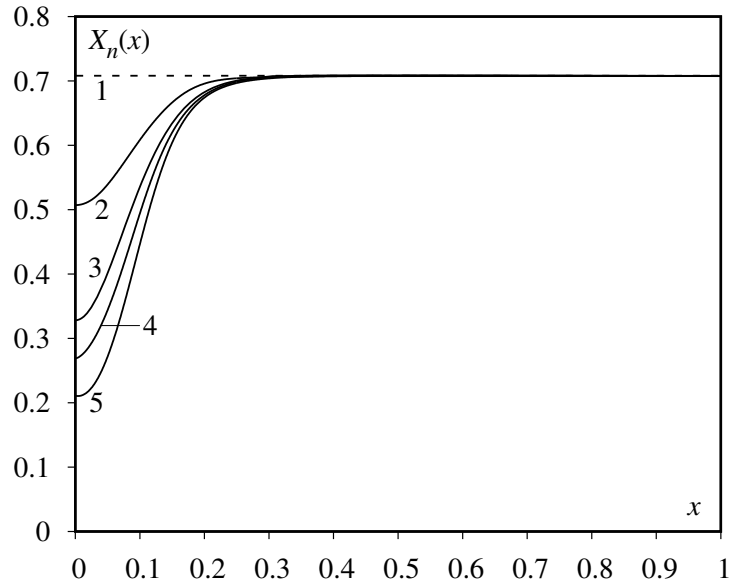
Figure 5. The partial distribution of hydrogen $X_n(x)$ in the Sun's core at different ages (see the text).

the zero age, curve 3 approximately corresponds to the current state of the Sun according to the calculations of Lamers & Levesque (2017). Curves 2, 4, and 5 are modeled to represent specific moments in the past and future. These curves are approximated using analytical expressions

$$X_n(x) = \left\{ \sum_{i=0}^{4} d_i^{(n)} x^i \right\}^{-1} \sum_{i=0}^{4} c_i^{(n)} x^i, \qquad (39)$$

and the coefficients $c_i^{(n)}$, $d_j^{(n)}$ for $n = 2, 3, 4$, and 5 are represented in Tab. 1. Curves $X_n(x)$ correspond to the radial dependence of the dimensionless molec-

Table 1. The coefficients of formula (39).

n	$c_0^{(n)}$	$c_1^{(n)}$	$c_2^{(n)}$	$c_3^{(n)}$	$c_4^{(n)}$
2	0.00121312	−0.0129071	0.159383	−0.899003	2.39018
3	0.000923382	−0.0036938	0.177201	−0.69752	3.856
4	0.00018172	0.0010917	0.0298524	−0.0866747	2.41146
5	0.000393233	−0.00373364	0.0869501	−0.45848	2.55274
n	$d_0^{(n)}$	$d_1^{(n)}$	$d_2^{(n)}$	$d_3^{(n)}$	$d_4^{(n)}$
2	0.00239208	−0.0253873	0.252826	−1.31403	3.40033
3	0.00281341	−0.0112101	0.248745	−0.961501	5.43149
4	0.000676466	0.00341449	0.0237693	−0.0889951	3.38885
5	0.00186471	−0.0157796	0.159344	−0.706516	3.63906

ular weight $\mu_n(r/R_\odot)$, calculated according to expression

$$\mu_n(x) = \{0.75 + 1.25\ X_n(x) - 0.005\}^{-1}. \tag{40}$$

Herewith, $\mu_1 = \bar{\mu}_1 = 0.6135$, and $\mu_3(x)$ is represented by expression (24). For the models with functions $\mu_2(x)$, $\mu_4(x)$, and $\mu_5(x)$ the solutions of equation (15) were found, and the values of α_n, β_n and γ_n were calculated. Additionally, the central density $\rho_c^{(n)}$, the moment of inertia I_n were determined and the age of the model t_n was evaluated. All these values are shown in Tab. 2. The values of the Sun's radius for the corresponding age were calculated according to the approximation formula

$$R_\odot(t) = R_\odot(k_0 + k_1 t), \tag{41}$$

where t is expressed in billions of years, $R_\odot = 6.963 \cdot 10^{10}$ cm is the radius of modern Sun. The coefficients $k_0 = 0.9545$ and $k_1 = 0.0101$ are determined based on the known value of $R_\odot$ and the radius value for zero age $R_\odot(0) = 6.646 \cdot 10^{10}$ cm (Sears, 1964).

As it was shown in Tab. 2, during the evolution of the Sun on the main sequence, its radius increases, there is a significant redistribution of matter along the radius and, as a result, the moment of inertia decreases. The change of the Sun mass during the existence on the main sequence is not taken into account. Therefore, according to the law of conservation of angular momentum, the decreasing of moment of inertia causes the relative increasing of the angular rotation velocity by an order of magnitude $(1 \div 3)\%$ for 10^9 years depending on the age.

Table 2. Evolutionary changes of the Sun characteristics (here $R_{\odot}^{(n)}$ is determined in units 10^{10}cm, $\rho_c^{(n)}$ – g cm^{-3}, I_n – 10^{53}g cm^2, and t – 10^9 years).

n	$X(0)$	$\xi_1^{(n)}$	α_n	β_n	γ_n	$R_{\odot}^{(n)}$	$\rho_c^{(n)}$	I_n	t
1	0.708	6.896	2.01824	10.8516	1.42891	6.646	87.610	6.6219	0
2	0.507	7.336	1.63094	9.34026	1.12159	6.805	121.634	6.5370	2.1379
3	0.328	7.951	1.29411	8.08539	0.85976	6.963	182.081	6.3527	4.5937
4	0.269	8.407	1.16195	7.68088	0.75303	7.091	227.076	6.2378	6.3085
5	0.211	9.274	1.00958	7.35792	0.62507	7.305	320.827	5.9967	9.3548

4. The star structure with rotation within the generalized model

In this section we consider a model of a star with constant velocity of axial rotation $\omega = $ const, which in the absence of rotation would have the characteristics of the modern Sun. Our aim is to compare characteristics of two rotating polytropes – standard and generalized, in particular, changes in their characteristics under the influence of rotation. To simplify the problem, we will take into account the effect of rotation within the perturbation theory.

The equilibrium equation of the star with axial rotation generalizes relation (5),

$$\nabla P(\mathbf{r}) = -\rho(\mathbf{r}) \ \{\nabla \ \Phi_{\text{grav}}(\mathbf{r}) + \nabla \Phi_{\text{c}}(\mathbf{r})\}. \tag{42}$$

In the spherical coordinate system with the axis of rotation directed along the Oz direction, the centrifugal potential is

$$\Phi_{\text{c}}(\mathbf{r}) = -\frac{1}{2} \ \omega^2 r^2 \sin^2 \theta, \tag{43}$$

where θ is the polar angle. Using the equation of state (3) and applying the gradient operator to both sides of equation (42), we obtain the analogue of equation (8)

$$4K\Delta \ \left(\frac{\rho(\mathbf{r})}{f(\mathbf{r})}\right)^{1/3} = -4\pi G\rho(\mathbf{r})f(\mathbf{r}) - f(\mathbf{r})\Delta\Phi_{\text{c}}(\mathbf{r}) - \\ - \left(\nabla f(\mathbf{r}), [\nabla\Phi_{\text{grav}}(\mathbf{r}) + \nabla\Phi_{\text{c}}(\mathbf{r})]\right). \tag{44}$$

At $f(\mathbf{r}) = 1$ this equations coincides with the equilibrium equation of a rotating polytrope. Since the last term on the right-hand side of equation (44) plays the role of correction, we consider it in the approximation of spherical symmetry,

following the same way as in formula (8)

$$4K\Delta\left(\frac{\rho(\mathbf{r})}{f(\mathbf{r})}\right)^{1/3} = -4\pi G\rho(\mathbf{r})f(\mathbf{r}) + 2\omega^2 f(\mathbf{r}) + \omega^2 r(1-z^2)\frac{\partial f(\mathbf{r})}{\partial r} -$$
$$- \frac{GM(\mathbf{r})}{r^2}\cdot\frac{\partial f(\mathbf{r})}{\partial r}, \tag{45}$$

where $z = \cos\theta$. Due to the fact that the influence of rotation is taken into account as a perturbation, we use a spherically symmetrical approximation for the function $f(\mathbf{r})$. We perform transition to the dimensionless variables by relations

$$r = \xi\lambda, \quad Y(\xi, z) = \left(\frac{\rho(\mathbf{r})}{f(\mathbf{r})}\cdot\frac{f_c}{\rho_c}\right)^{1/3}, \tag{46}$$

using the same scale as for the model without rotation. Introducing the dimensionless angular velocity

$$\Omega = \omega\left(\frac{f_c}{2\pi G\rho_c}\right)^{1/2}, \tag{47}$$

we transform equation (45) to the dimensionless form

$$\Delta_{\xi,z}Y(\xi, z) = \Omega^2 f(\xi/\xi_1) - Y^3(\xi, z)f^2(\xi/\xi_1) +$$
$$+ \frac{\Omega^2}{2}\cdot\frac{\xi}{\xi_1}(1-z^2)\frac{\partial f(\xi/\xi_1)}{\partial(\xi/\xi_1)} - \frac{f_c}{\xi_1\xi^2}\cdot\frac{\partial f(\xi/\xi_1)}{\partial(\xi/\xi_1)}\int\limits_0^{\xi}(\xi')^2 y^3(\xi')\frac{\mu(\xi'/\xi_1)}{\mu(0)}d\xi'. \tag{48}$$

Here

$$\Delta_{\xi,z} = \Delta_{\xi} + \xi^{-2}\Delta_z;$$
$$\Delta_{\xi} = \frac{\partial^2}{\partial\xi^2} + 2\xi^{-1}\frac{\partial}{\partial\xi}; \quad \Delta_z = \frac{\partial}{\partial z}(1-z^2)\frac{\partial}{\partial z}. \tag{49}$$

The substitution

$$Y(\xi, z) = y(\xi) + \Omega^2\Psi(\xi, z) \tag{50}$$

and linearization of equation for the function $\Psi(\xi, z)$ predicts that the generalized polytrope, without rotation, is used in the role of a zero approximation for calculating characteristics of a rotating polytrope. In such approximation $\Psi(\xi, z)$ satisfies the equation

$$\Delta\Psi(\xi, z) = f(\xi/\xi_1) + \xi(3\xi_1)^{-1}\left(1 - P_2(z)\right)\frac{\partial}{\partial(\xi/\xi_1)}f(\xi/\xi_1) -$$
$$- 3y^2(\xi)f^2(\xi/\xi_1)\Psi(\xi, z), \tag{51}$$

where $P_2(z)$ is the Legendre polynomial of second order and $y(\xi)$ is the solution of equation (15). From equation (51) it follows that $\Psi(\xi, z)$ can be represented

in the form of expansion in a series of Legendre polynomials (Abramowitz & Stegun, 1970),

$$\Psi(\xi, z) = \psi_0(\xi) + \sum_{l \geq 1}^{\infty} a_{2l} P_{2l}(z) \psi_{2l}(\xi), \tag{52}$$

where a_{2l} are integration constants. By substituting series (52) into equation (51) and equating the multipliers with the same Legendre polynomials, we obtain the system of independent linear equations for functions $\psi_0(\xi)$ and $\psi_{2l}\xi$

$$\Delta_\xi \psi_0(\xi) = f(\xi/\xi_1) - 3y^2(\xi)f^2(\xi/\xi_1)\psi_0(\xi) + (3\xi_1)^{-1}\xi\frac{\partial}{\partial(\xi/\xi_1)}f(\xi/\xi_1);$$

$$\Delta_\xi \psi_2(\xi) = \left\{ \frac{6}{\xi^2} - 3y^2(\xi)f^2(\xi/\xi_1) \right\} \psi_2(\xi) - $$

$$- (3a_2\xi_1)^{-1}\frac{\partial}{\partial(\xi/\xi_1)}f(\xi/\xi_1);$$

$$\Delta_\xi \psi_{2l}(\xi) = \left\{ \frac{2l(2l+1)}{\xi^2} - 3y^2(\xi)f^{\,2}(\xi/\xi_1) \right\} \psi_{2l}(\xi), \dots \tag{53}$$

for $l \geq 2$. For $f(\xi/\xi_1) = 1$ these equations coincide with the equations for the standard rotational polytrope with $n = 3$ (Vavrukh et al., 2020). According to the definition of the function $Y(\xi, z)$ and conditions (16), equations (53) correspond to the boundary conditions

$$\psi_{2l}(0) = 0, \quad \frac{\partial}{\partial\xi}\psi_{2l}(\xi) = 0 \quad \text{at } \xi = 0 \text{ for } l \geq 0. \tag{54}$$

It's easy to see that the function $\psi_0(\xi)$ has asymptotics $f(0)\xi^2/6 + \dots$ for $\xi \ll 1$, and functions $\psi_{2l}(\xi)$ for $l \geq 1$ are convenient by normalized to the Bessel functions of the first kind (Abramowitz & Stegun, 1970) $(\psi_{2l}(\xi) \Rightarrow [(2l+1)!!]^{-1}\xi^{2l} + \dots)$. In Figs. 6 and 7 we compare the solutions of equations $\psi_0(\xi)$ and $\psi_2(\xi)$ for both the standard and the generalized rotational polytropes.

The expression

$$\rho_1(\xi, z) = \rho_c \frac{f(\xi/\xi_1)}{f_c} \left\{ y(\xi) + \Omega^2\Psi(\xi, z) \right\}^3 \tag{55}$$

determines the distribution of matter in the rotational generalized polytrope, and the expression

$$\rho_0(\xi, z) = \rho_c^{(0)} \left\{ y_3(\xi) + \Omega_0^2\Psi^{(0)}(\xi, z) \right\}^3 \tag{56}$$

yields the analogous distribution for the standard rotational polytrope. Herewith, $\Omega_0 = \omega(2\pi G\rho_c^{(0)})^{-1/2}$

$$\Psi^{(0)}(\xi, z) = \psi_0^{(0)}(\xi) + \sum_{l \geq 1} a_{2l}^{(0)}\psi_{2l}^{(0)}(\xi)P_{2l}(z), \tag{57}$$
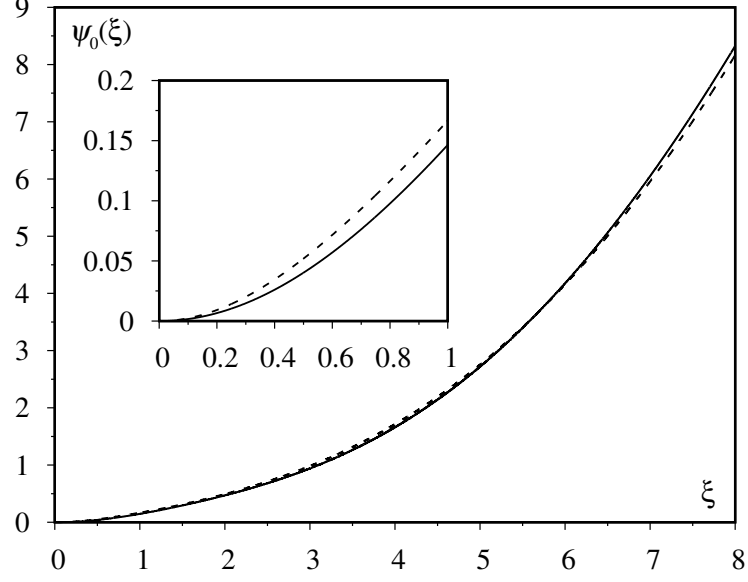
Figure 6. Dependence of the function $\psi_0(\xi)$ on the variable ξ. The solid curve corresponds to the standard model, the dashed one – to the generalized model.

and functions $\psi_0^{(0)}(\xi)$, $\psi_{2l}^{(0)}(\xi)$ are determined by equations (53), in which the replacements $f(\xi/\xi_1) \Rightarrow 1$ and $y(\xi) \Rightarrow y_3(\xi)$ should be performed.

In the case of small angular velocities, integration constants a_{2l} and $a_{2l}^{(0)}$ can be determined using the Milne-Chandrasekhar method (Milne, 1923) based on the condition of continuity of the gravitational potential on the star's surface. Constants a_2 and $a_2^{(0)}$ corresponding to the generalized and the standard models are determined by the following expressions

$$
a_2 = -\frac{5}{6}\xi_1^2 \left\{ 3\psi_2(\xi_1) + \xi_1 \frac{\partial}{\partial \xi_1}\psi_2(\xi_1) \right\}^{-1},
$$
$$
a_2^{(0)} = -\frac{5}{6}(\xi_1^{(0)})^2 \left\{ 3\psi_2^{(0)}(\xi_1^{(0)}) + \xi_1^{(0)} \frac{\partial}{\partial \xi_1^{(0)}}\psi_2^{(0)}(\xi_1^{(0)}) \right\}^{-1},
$$

$$(58)$$

where $\xi_1^{(0)} = 6.89685\ldots$ is the dimensionless radius of the standard model without rotation. Note that in expressions (55) and (56), the central densities of corresponding polytropes without rotation appear.

The surface of rotational polytropes is determined in the following way. The conditions

$$
Y(\xi, 1) = 0 \quad \text{and} \quad Y(\xi, 0) = 0 \tag{59}
$$
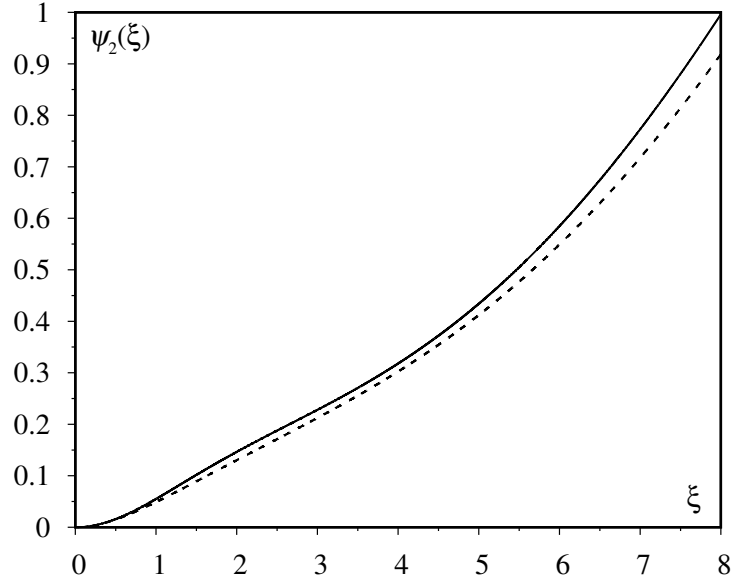
Figure 7. Dependence of the function $\psi_2(\xi)$ on the variable ξ. The notations are the same as in the previous figure.

determine polar and equatorial radii of the generalized rotational polytrope $\xi_p(\Omega)$ and $\xi_e(\Omega)$. Taking into account that the surface of the rotational polytrope is close to the surface of a rotational ellipsoid, the surface equation of the polytrope can be rewritten in the form

$$\xi_1(z) = \xi_e(\Omega) \left\{ 1 + z^2 \frac{e^2(\Omega)}{1 - e^2(\Omega)} \right\}^{-1/2}, \tag{60}$$

where

$$e(\Omega) = \left\{ 1 - \left(\frac{\xi_p(\Omega)}{\xi_e(\Omega)} \right)^2 \right\}^{1/2} \tag{61}$$

is the eccentricity of the ellipsoid. In the case of the standard polytrope, we should make the replacement $\Omega \to \Omega_0$.

The dimensionless angular velocity Ω is an independent parameter of the problem. Its maximal value $\Omega_{\max}$ is determined by the conditions of the violation of monotonous behavior of the function $Y(\xi, z)$ at the star's equator

$$Y(\xi, 0) = 0, \quad \frac{\partial}{\partial \xi} Y(\xi, 0) = 0, \tag{62}$$

which also determines the maximal value of the equatorial radius according to condition (59). For $\Omega > \Omega_{\max}$, there occurs a leakage of matter at the equator. For the standard model of a rotational polytrope with $n = 3$ we obtain the value that is close to $\Omega_{\max}^{(0)} = 0.0623$ (Vavrukh et al., 2020). In the case of the generalized polytrope, this value depends on the function $f(r/R)$. For the model that is close to the modern Sun, $\Omega_{\max} \approx 0.047\ldots$.

The values of polar and equatorial radii, as well as the eccentricity as functions of angular velocity in the interval $0 \leq \Omega \leq \Omega_{\max}$ are shown in Tab. 3.

Table 3. Dependence of the macroscopic characteristics of the generalized polytrope on the angular velocity Ω.

Ω	$\xi_p(\Omega)$	$\xi_e(\Omega)$	$e(\Omega)$	$\eta(\Omega)$
0.010	7.94171	8.0049	0.12540	1.00196
0.020	7.90259	8.16825	0.25296	1.00795
0.030	7.83899	8.50059	0.38678	1.01832
0.040	7.75314	9.21084	0.53988	1.03384
0.041	7.74343	9.33013	0.55786	1.03572
0.042	7.73353	9.46723	0.57682	1.03768
0.043	7.72344	9.62809	0.59701	1.03970
0.044	7.71317	9.82262	0.61918	1.0418
0.045	7.70271	10.0695	0.64408	1.04398
0.046	7.69207	10.4125	0.67400	1.04624
0.047	7.68126	11.0316	0.71775	1.04859

According to expression (55) the total mass of the generalized polytrope can be rewritten in the form

$$M(\Omega) = 2\pi\lambda^3\rho_c \int\limits_{-1}^{+1} dz \int\limits_{0}^{\xi_1(z)} \xi^2 \frac{f(\xi/\xi_1)}{f(0)}\{y(\xi) + \Omega^2\Psi(\xi, z)\}^3 d\xi. \qquad (63)$$

In Tab. 3 there is also shown the ratio

$$\eta(\Omega) = M(\Omega) \cdot M_3^{-1}, \qquad (64)$$

where M_3 is the mass of the generalized polytrope without rotation. In Fig. 8 there is shown the dependence of polar and equatorial radii for two rotational polytropes: the standard one with angular velocity Ω_0 and the generalized one with angular velocity Ω. The increase in the equatorial radius of the generalized polytrope under the influence of rotation is several times greater than the similar change for the standard polytrope.
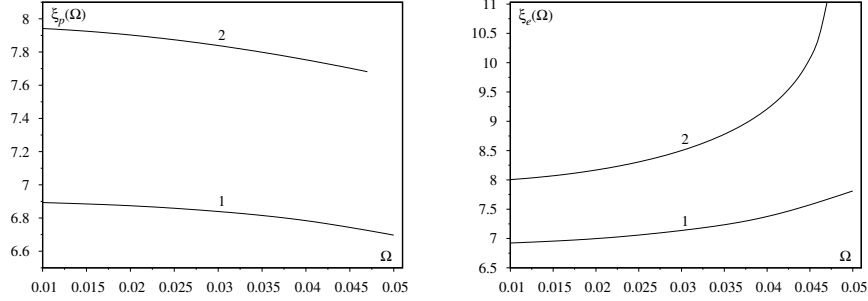
Figure 8. Dependence of polar and equatorial radii on the angular velocity in different approximations. Curves 1 correspond to the results of Vavrukh et al. (2020), curves 2 – to the generalized polytropic model.

5. Conclusions

1. The generalized polytropic model of stars with a spatially heterogeneous distribution of chemical composition, created by thermonuclear reactions, was substantiated using the Eddington method. This is manifested in the radial dependence of the dimensionless effective molecular weight. The standard polytropic model with $n = 3$ represents the limiting case when $f(r) = 1$ and corresponds to a star of zero age. This is confirmed through the calculation of characteristics of the Sun within both the standard and generalized models, and the comparison with the results of calculating the Sun's characteristics at zero age and in the modern epoch based on the Schwarzschild equations (Schwarzschild, 1958).

2. Modeling the radial distribution of partial density of hydrogen also allows us to calculate the evolutionary characteristics of the star, which are shown in Table 2. The table provides the central density, radius, and moment of inertia of the Sun at different epochs.

3. As shown in Section 4, the influence of rotation in the generalized polytropic model leads to much greater changes in mass, polar, and especially equatorial radii than in the case of the standard rotational polytrope. For example, for the maximal value of the dimensionless angular velocity ($\Omega_{\mathrm{max}} = 0.047\ldots$), the increase of mass and equatorial radius due to rotation is almost 3 times greater than in the standard rotational polytrope.

4. The calculations demonstrate the significant advantages of the generalized polytropic model. The results of Chandrasekhar (1933), James (1964), Caimmi (1980), Williams (1988), Kong et al. (2015), Knopik et al. (2017) and Vavrukh et al. (2020), which are based on the standard rotational polytropic model, correspond to stars with zero age and have a limited field of application.

References

Abramowitz, M. & Stegun, I. A. 1970, *Handbook of mathematical functions: with formulas, graphs, and mathematical tables*

Caimmi, R., Emden-Chandrasekhar Axisymmetric Solid-Body Rotating Polytropes - Part One - Exact Solutions for the Special Cases N=O, 1 and 5. 1980, *Astrophysics and Space Science*, **71**, 415, DOI: 10.1007/BF00639402

Chandrasekhar, S., The equilibrium of distorted polytropes. I. The rotational problem. 1933, *Monthly Notices of the RAS*, **93**, 390, DOI: 10.1093/mnras/93.5.390

Eddington, A. S. 1988, *The Internal Constitution of the Stars* (Cambridge University Press)

James, R. A., The Structure and Stability of Rotating Gas Masses. 1964, *Astrophysical Journal*, **140**, 552, DOI: 10.1086/147949

Knopik, J., Mach, P., & Odrzywołek, A., The shape of a rapidly rotating polytrope with index unity. 2017, *Monthly Notices of the Royal Astronomical Society*, **467**, 4965, DOI: 10.1093/mnras/stx164

Kong, D., Zhang, K., & Schubert, G., An exact solution for arbitrarily rotating gaseous polytropes with index unity. 2015, *Monthly Notices of the Royal Astronomical Society*, **448**, 456, DOI: 10.1093/mnras/stu2759

Lamers, H. J. G. L. M. & Levesque, E. M. 2017, *Understanding Stellar Evolution* (IOP Publishing)

Milne, E. A., The equilibrium of a rotating star. 1923, *Monthly Notices of the RAS*, **83**, 118, DOI: 10.1093/mnras/83.3.118

Monaghan, J. J. & Roxburgh, I. W., The structure of rapidly rotating polytropes. 1965, *Monthly Notices of the Royal Astronomical Society*, **131**, 13, DOI: 10.1093/mnras/131.1.13

Schwarzschild, M. 1958, *Structure and Evolution of the Stars* (Princeton University Press)

Sears, R. L., Helium Content and Neutrino Fluxes in Solar Models. 1964, *Astrophysical Journal*, **140**, 477, DOI: 10.1086/147942

Vavrukh, M. V., Tyshko, N. L., & Dzikovskyi, D. V., New approach in the theory of stellar equilibrium with axial rotation. 2020, *Journal of Physical Studies*, **24**, 3902, DOI: 10.30970/jps.24.3902

Williams, P. S., Analytical Solutions for the Rotating Polytrope N=1. 1988, *Astrophysics and Space Science*, **143**, 349, DOI: 10.1007/BF00637146

The computer programs to check the internal consistency of the meteor-shower data

L. Neslušan[1] , **R. Rudawska**[2] , **M. Hajduková**[3] , **S. Ďurišová**[3] and **T.J. Jopek**[4]

[1] *Astronomical Institute of the Slovak Academy of Sciences*
059 60 Tatranská Lomnica, The Slovak Republic, (E-mail: ne@ta3.sk)
[2] *RHEA Systems / ESA ESTEC, Noordwijk, the Netherlands*
[3] *Astronomical Institute of the Slovak Academy of Sciences, Interplanetary Matter Division, Dúbravská cesta 9, 845 04 Bratislava, The Slovak Republic*
[4] *Astronomical Observatory Institute, Faculty of Physics, A. M. University, Poznań, Poland*

Abstract. At times, it becomes necessary to verify the internal consistency of meteor shower characteristics, regardless they are one's own observations or information taken from the literature. A check of internal consistency also appears desirable when the shower characteristics are reported to the Meteor Data Center (MDC) of the International Astronomical Union (IAU). In this article, we describe and provide software that we have developed, which is capable of performing checks of internal consistency between the mean geocentric parameters (solar longitude, geocentric radiant, and geocentric velocity) and mean orbital elements (perihelion distance, eccentricity, argument of perihelion, longitude of ascending node, and inclination) of a shower or several showers. The program is freely accessible (Fortran77 source code as well as executable static binary code) along with this article or from the IAU MDC web pages.
Key words: meteor showers – geocentric parameters – orbital elements – meteoroid data verification – software

1. Introduction

The Meteor Data Center of the International Astronomical Union (IAU MDC, hereafter) provides, via its web site (https://www.iaumeteordatacenter.org/), both individual meteoroids (Orbital Database) and meteor shower data (Shower Database), see Rudawska et al. (2021). These data include, with some exceptions concerning the meteor showers, both geocentric and heliocentric parameters. There is a close relationship between geocentric and heliocentric parameters for individual meteoroids. The latter are calculated using the values of the geocentric parameters. Here we also have the possibility of performing inverse calculations. Thus, for geocentric and heliocentric individual meteoroid data given in

the literature or online catalogs, we have the opportunity to check their mutual consistency. In the past and quite recently, such a check has been done many times, both for photographic and radio data, e.g. by Jopek (1986, 1991); Jopek et al. (2003); Koseki (1986); Lindblad (1991, 1992); Lindblad et al. (2001, 2003); Svoreň et al. (2008); Neslušan et al. (2012, 2014). It turned out that for several hundred meteoroids there were various types of numerical inconsistencies, which show how important it is to verify individual meteoroid data.

It would, therefore, be expected that inconsistencies may be encountered for a part of the data of meteoroid streams listed in the IAU MDC. One shower in the MDC can be reported by more than a single author team; each report of shower is regarded as its "solution". As far as we know, with the exception of Koseki (2016), the verification of the internal consistency of the meteor shower solution's characteristics given in the IAU MDC has never taken place. We are referring here to the internal inconsistency of the data and not to the errors we corrected in Hajduková et al. (2023), which were related to differences between submitted parameters and their values in the source publications. To this end, we would like to use a method similar to that used for testing individual meteoroid data.

However, in the case of meteoroid streams, a close relationship between the mean geocentric and heliocentric parameters is most often not the case. Usually, mean values of geocentric and heliocentric parameters are calculated separately, as arithmetic means of individual meteoroid parameters, members of a given stream. This causes some difficulties in verifying the meteoroid stream data. Therefore, we are forced to use a procedure of approximate nature.

In the following sections, we describe the method for assessing the internal consistency of meteoroid stream data and the resulting software for determining such consistency.

2. Calculation of geocentric parameters

In the following, we consider a hypothetical "mean meteoroid" moving in the mean orbit of a given meteoroid stream. If the mean orbital elements, perihelion distance, q, eccentricity, e, argument of perihelion, ω, longitude of ascending node, Ω, and inclination, i, are known, then it is possible to find the point of the mean orbit, where the mean meteoroid approaches the Earth's orbit, and next, to calculate the meteor's geocentric radiant, geocentric velocity, and solar longitude of the point of approach. The calculated values can be compared with their observed counterparts given in the IAU MDC list. A significant difference between the corresponding values indicates an inconsistency in the data.

In the past, as well as sometimes nowadays, it is assumed that the orbit of each meteoroid colliding with the Earth must cross the orbit of our planet. In general, this is not true, but in the past, and perhaps even now, some authors, when calculating the orbit of a meteoroid, make this assumption which simpli-

fies the calculation process. Precise calculations also require knowledge of the observed position of the meteoroid relative to the center of the Earth.

However, the aforementioned assumption is definitely not met for the mean orbit of a stream, which is calculated as a simple arithmetic average of a given element of all individual meteoroids belonging to the stream. Hence, to calculate the mean shower's geocentric parameters more simply, the known mean orbit of the stream has to be modified to achieve the crossing of the Earth's orbit. This modification was carried out by the most appropriate of six methods, which were also considered in creating the computer program that calculates the meteor radiant (Neslušan et al., 1998). The most appropriate method provides us with the crossing point of both meteoroid and Earth orbits and, hence, with the date in the year when the crossing happens.

There is, however, a difference between the calculation of the position of Earth in the case of an individual meteoroid and the mean meteoroid. The mean orbit of a stream is often calculated based on the meteor data collected during a period spanning several years. Even in a single year, the position of this planet is different at the moments of the fall of individual members of the stream. In the case of a mean meteoroid, its exact time of fall cannot be found. We can determine only the mean solar longitude in a specific year. We chose the year 2000. Since the mean orbits of known streams have been determined in the twentieth and twenty-first centuries, the choice of the fixed year does not result in a significant deviation in the Earth's position since its orbit changes negligibly during about two centuries.

When the crossing point is recognized, by one of the six considered methods, we know the true anomaly of the mean meteoroid at this point; therefore, we can calculate the components of its heliocentric velocity vector, $\boldsymbol{V}_h$. At the crossing point, the Earth's heliocentric velocity vector, $\boldsymbol{V}_E$, is also known. From these two vectors, the geocentric velocity vector, $\boldsymbol{V}_g$, of the mean meteoroid can be calculated as

$$\boldsymbol{V}_g = \boldsymbol{V}_E - \boldsymbol{V}_h, \tag{1}$$

whereby the direction to the radiant is pointed out by vector $-\boldsymbol{V}_g$.

At the crossing point, the ecliptic longitude, λ_E, and the heliocentric radius vector of the Earth, $\boldsymbol{r}_E$, which is identical with the heliocentric radius vector of the mean meteoroid are also known; while the moment of activity of a meteor swarm is represented by the corresponding solar ecliptic longitude $\lambda_\odot$

$$\lambda_\odot = \lambda_E + 180°, \tag{2}$$

and the magnitude of the mean meteoroid's geocentric velocity (in [au/day]) can be calculated as

$$V_g = k\sqrt{M_\odot}\sqrt{\frac{2}{r_E} - \frac{1-e}{q}}, \tag{3}$$

where k is the Gauss gravitational constant.

The geocentric parameters, solar longitude, right ascension and declination of the geocentric radiant and the geocentric velocity are calculated in the above-outlined way by the program *radiants.f*. Before using it, one has to prepare the input data file (its default name is *allshowers11jan2023.db*; the name can, however, be defined in the input-parameter file *inparams.rad*, see below). The structure of this file should remain constant. The file should contain the mean parameters of all showers to be checked. The data on each shower must be given in one line, whereby the data are arranged in order:

IAU No. of the shower (IAU shower number),

additional number (AdNo.) of the solution of the shower,

mean solar longitude [deg],

mean right ascension of geocentric radiant [deg],

mean declination of geocentric radiant [deg],

mean geocentric velocity [km s^{-1}],

mean perihelion distance [au],

mean eccentricity [1],

mean argument of perihelion [deg],

mean longitude of ascending node [deg],

mean inclination [deg], and

number of meteors in a given solution (if unknown give -1).

Before the run of the *radiants* program, another input file, *inparams.rad*, must be prepared. In this file, we can define the names of the files with the input and output data and the acceptable difference (tolerance) of the checked parameters. Namely, the values calculated by the original author and by us are expected to differ because of various reasons, such as using different methods of radiant determination, calculation of the position of the Earth in different years, etc. For example, if we choose the tolerance for the right ascension of the geocentric radiant equal to 3°, only the difference larger than 3° between the original and our calculated values will occur in the list of the differences given in their output file (see below). Each value that should be given in *inparams.rad* is described in the previous line of this file.

After running the program *radiants*, two (or three) output files will occur. Their default names are *check_orb.d* and *errors_geo.inf* (but the user can define other names in the file *inparams.rad* if they wish). In the file *check_geo.d*, there is a list of the following geocentric quantities of all considered shower solutions:

serial number of solution,

IAU No. of the shower,

additional number (AdNo.) characterizing the particular solution of the shower,

solar longitude [deg],

right ascension of geocentric radiant [deg],

declination of geocentric radiant [deg],

geocentric velocity [km s^{-1}],

and the method of the modification of orbit to cross the orbit of the Earth (Q, B, W, A, H, P; the description can be found in (Neslušan et al., 1998)).
IAU No. and AdNo. are the unique identification codes of a given solution. (Unfortunately, in a few cases the AdNo. was changed in the past versions of the MDC list; it is fixed from January 1, 2024.)

The geocentric parameters are given in two lines, whereby the values published by the original author are in the first and the values calculated by the program are in the second line. See below an example, an extract of the content of the file *check_geo.d*:

```
Example 1 (check_geo.d):

ser.No. IAU AdNo  LS       RA       DEC      Vg    method
-----------------------------------------------------------
   1     1  0   128.900  306.600   -8.200  22.200
               129.283  306.446   -8.364  22.108   H

   2     1  1   122.300  306.700   -9.300  23.400
               122.415  303.344  -10.024  23.127   H

   3     1  3   127.660  307.680   -9.920  22.800
               128.803  307.258   -9.354  22.381   H

   4     1  4   127.900  307.100   -8.900  22.600
               127.922  306.675   -9.041  22.520   H

   5     1  5   123.300  302.900   -9.900  22.200
               123.238  302.609  -10.012  22.137   H

   6     1  8   125.400  306.500   -9.200  23.000
               125.028  304.328   -9.654  22.806   H

   7    1 10   115.200  300.000  -11.900  25.000
               115.231  299.651  -12.028  24.880   H

   8    1 11   124.100  304.300   -9.900  23.200
               124.100  303.947   -9.947  23.135   A

   9    1 12   130.400  307.700   -8.300  21.900
               130.491  307.161   -8.328  21.740   H

  10     2  0   217.300   48.700   13.000  28.000
               217.364   49.464   13.390  27.722   H
```

```
11      2  1   207.600    40.600    10.300   27.800
               208.021    41.619    10.677   27.451    H

12      2  2   221.500    51.700    14.000   28.200
               221.646    52.242    14.113   28.015    H

13      2  3   196.000    31.000     8.000   27.920
               196.062    30.613     9.866   27.633    H

14      2  5    16.000    30.900     8.100   28.200
               195.973    31.225     8.159   27.922    H

15      2  6    34.400    47.900    12.800   26.600
               214.081    47.253    12.711   26.551    H

16      2  8   224.500    54.900    14.600   28.000
               224.580    55.520    14.748   27.726    H

17      2  9    22.400    36.800     9.700   28.600
               200.505    36.183     9.765   29.489    Q

18      2 10    41.600    51.800    13.700   27.400
               221.576    52.436    13.900   27.190    H

19      2 11   242.100    65.300    14.900   23.400
               242.125    65.619    15.067   23.351    H

20      2 12    85.100    82.900    14.900   20.600
               264.973    82.962    15.091   20.566    H
```

The found differences in the verified parameters, larger than the defined tolerances (by the user in file *inparams.rad*), are written into the output file *errors_geo.inf*. Each difference is given in one line, which contains the IAU No. of the shower, the AdNo. of its solution, the value of the parameter published by the original author ("observed" value), and the value of this parameter as re-calculated by the program. There can be several wrong parameters in one shower solution, therefore the differences for this solution are then written in several lines. See below an example, an extract of the file *errors_geo.inf*:

```
Example 2 (errors_geo.inf):

IAU No. =   11  AdNo. =  0  V_g_orig = 36.000  V_g_rec. = 33.806
IAU No. =   11  AdNo. =  1   LS_orig = 280.50   LS_rec. = 339.90
```

```
IAU No. =    11  AdNo. =  1   RA_orig = 182.10   RA_rec. = 170.67
IAU No. =    11  AdNo. =  1  DEC_orig =   2.60  DEC_rec. =   5.73
IAU No. =    16  AdNo. =  3   RA_orig = 134.40   RA_rec. = 128.67
IAU No. =    16  AdNo. =  3  V_g_orig = 58.900  V_g_rec. = 55.880
IAU No. =    18  AdNo. =  4   LS_orig = 231.10   LS_rec. = 320.92
IAU No. =    18  AdNo. =  4   RA_orig =  21.70   RA_rec. = 133.03
IAU No. =    18  AdNo. =  4  DEC_orig =  33.50  DEC_rec. =  39.84
IAU No. =    21  AdNo. =  0  V_g_orig = 20.000  V_g_rec. = 17.010
IAU No. =    21  AdNo. =  4  DEC_orig =   2.90  DEC_rec. =   6.16
IAU No. =    21  AdNo. =  4  V_g_orig = 18.800  V_g_rec. = 16.898
```

Sometimes, there is a need to know the geophysical parameters determined by every method used to modify the mean orbit. The user can specify such a request in the input file *inparams.rad*, writing another, extensive, output file, which is named by the program *debug.d*.

For every shower solution, there is given the minimum-orbit intersection distance (MOID) between the orbit of the Earth and the post-perihelion and pre-perihelion arcs of the solution orbit, and all calculated parameters, when the known orbit of the solution is modified to exactly cross the Earth's orbit, by each of the six methods used (Q, B, W, A, H, and P; see (Neslušan et al., 1998)). In more detail, there are three values of each parameter also listed in the input data file: the value published by the original author, the value calculated by the program for the node on the post-perihelion arc, and the value calculated by the program for the node on the pre-perihelion arc of the mean orbit of the solution. The Southworth & Hawkins (1963) *D* criterion between the originally published mean orbit and the modified orbit crossing the orbit of our planet in the first or second node is also given along with the heliocentric speed.

An example of a part of the *debug.d* file for one solution and one method of the modification of the mean orbit is below.

```
Example 3 (debug.d):

IAU No. =   1  AdNo. =  0
   MOID:              0.0214  0.0009
    P-method:
D_1, D_2:              0.026   0.001
q:           0.602   0.600   0.602
e:           0.770   0.771   0.770
arg.:      266.670 275.943 266.292
node:      128.900 119.773 129.272
i:           7.680   6.716   7.643
lambda_sun: 128.900 299.773 129.272
R.A.:      306.600 306.273 307.237
```

```
DEC.:          -8.200 -28.949  -8.330
V_g:           22.200  22.322  22.332
V_h(calc.):            38.267  37.542
```

3. Calculation of orbital elements

We again consider a hypothetical "mean meteoroid" moving in the mean orbit of a given meteoroid stream. This time, the mean geocentric parameters, solar longitude, $\lambda_\odot$, right ascension, α, and declination, δ, of geocentric radiant, and geocentric velocity, V_g, are known and a program named *elements.f* calculates the orbital elements, perihelion distance, q, eccentricity, e, argument of perihelion, ω, longitude of ascending node, Ω, and inclination, i.

It is the inverse calculation with respect to that performed by the program *radiants.f*. Both calculations are useful. Sometimes, the cause of a large difference cannot be revealed by the first program but can be revealed by the second program. For example, if there is a typing error in the mean argument of perihelion of a solution, we obtain all calculated geocentric parameters significantly different from those published by the original author. However, the inverse calculation of orbital elements results only in a difference in the argument of perihelion.

The names of input and output files as well as the tolerance in the checked orbital elements can be specified when one wants to use a program *elements*, in the input file *inparams.ele*. The input data file, with all mean parameters for all checked shower solutions, is identical with the input data file for the program *radiant* (its default name is *allshowers11jan2023.db*).

There are again two output files created by the program *elements*. Their default names are *check_orb.d* and *errors_orb.inf* (they can be changed in the file *inparams.ele*). File *check_orb.d* contains the re-calculated orbital elements for every solution. In the individual columns of this file, there are given: serial number of the given solution, IAU No. of the shower, number of its solution, perihelion distance, eccentricity, argument of perihelion, longitude of ascending node, and inclination. The orbital elements are written in two lines. While the values published by the original author can be seen in the first line, the values calculated by the program *elements* are in the second line. See below an extract of the content of the file *check_orb.d*:

```
Example 4 (check_orb.d):

ser.No. IAU AdNo  q         e        arg.     node       i
--------------------------------------------------------------
      1    1  0  0.60200  0.77010  266.670  128.900    7.680
                 0.59710  0.75842  267.403  128.078    7.860
```

```
2     1  1  0.55000  0.76800  273.300  122.300    7.700
              0.50719  0.74188  280.113  121.678    8.125

3     1  3  0.59000  0.77000  269.000  127.660    7.000
              0.56579  0.76247  271.335  126.914    6.796

4     1  4  0.58600  0.77000  268.400  127.900    7.400
              0.57631  0.75969  270.079  127.107    7.538

5     1  5  0.58600  0.75000  269.200  123.300    7.300
              0.58152  0.74559  270.044  122.841    7.394
```

Output data file with the default name *errors_.inf* contains the list of values which differ more than the specified tolerance. Again, one wrong parameter is written in one line. The line consists of the IAU No. of the shower, the AdNo. of its solution, the value of the parameter published by the original author ("observed" value), and the corresponding value calculated by the program *elements*. See below an extract of the content of the file *errors_orb.inf*:

```
Example 5 (errors_orb.inf):

IAU No. =    1 AdNo. =  1  arg_orig = 273.3  arg_rec. = 280.1
IAU No. =    2 AdNo. =  3    i_orig =   3.0    i_rec. =   5.5
IAU No. =    5 AdNo. =  0    i_orig =  30.8    i_rec. =  28.0
IAU No. =    5 AdNo. =  3    i_orig =  27.2    i_rec. =  17.2
IAU No. =    5 AdNo. =  3  arg_orig = 152.8  arg_rec. = 146.5
IAU No. =    6 AdNo. =  2    e_orig = 0.968    e_rec. = 1.057
IAU No. =   11 AdNo. =  1    q_orig = 0.382    q_rec. = 0.003
IAU No. =   11 AdNo. =  1    e_orig = 0.851    e_rec. = 0.994
IAU No. =   11 AdNo. =  1    i_orig =   3.5    i_rec. =  46.9
IAU No. =   11 AdNo. =  1  arg_orig = 349.1  arg_rec. = 359.3
IAU No. =   13 AdNo. =  4  arg_orig = 172.3  arg_rec. = 166.9
IAU No. =   13 AdNo. =  7  arg_orig = 171.1  arg_rec. = 164.8
IAU No. =   13 AdNo. =  8  arg_orig = 170.8  arg_rec. = 165.7
IAU No. =   16 AdNo. =  3  nod_orig =  76.5  nod_rec. =  85.4
IAU No. =   17 AdNo. =  0    q_orig = 0.350    q_rec. = 0.296
IAU No. =   17 AdNo. =  0  arg_orig = 294.9  arg_rec. = 303.9
IAU No. =   18 AdNo. =  4  nod_orig = 321.1  nod_rec. = 229.6
IAU No. =   20 AdNo. =  6    e_orig = 0.810    e_rec. = 0.757
```

4. Types of the differences

Both introduced programs should serve to reveal significant internal inconsistencies in the meteor shower data. The user alone must however define what a difference in a given parameter should be regarded as a discrepancy, i.e. they must set the tolerance limit. A good choice of tolerance limits can be made with the help of the distributions of the absolute values of differences in the checked set of parameters which are shown in Figs. 1 (geocentric parameters) and 2 (orbital elements). In more detail, these figures show the distributions of the differences of checked parameters between the values as given in the MDC list and those calculated by us using the programs. When selecting tolerance limits, none should be overly strict to avoid the detection of many acceptable differences. In the calculation resulting in the examples presented above, the tolerance in declination of radiant and inclination of orbit was $2.5°$, and the tolerance in the other angular elements $5°$. The tolerance in geocentric velocity (perihelion distance and eccentricity) was $1.5\,\mathrm{km\,s}^{-1}$ ($0.05\,\mathrm{au}$ and 0.05).

On the other hand, the checking of consistency would not be very accurate (will not serve its purpose) if the tolerance was too large. When compromising, a difference of a parameter may only slightly exceed the tolerance limit, and the published value can, thus, be still acceptable. For example, the published mean inclination of solution AdNo. 3 of the shower with the IAU No. 2 (the second line in Example 5 above) is $3°$ and the calculated inclination is $5.543°$. The difference is $2.543°$, which exceeds the tolerance in inclination of $2.5°$ only about $0.043°$. This is not a significant difference; the solution can be regarded as correct.

In Fig. 2d, we can see that the number of showers does not decrease with the increasing difference, but there is a peak at the difference $\Delta\Omega \approx 2°$. Our analysis revealed that this peak occurs because many authors considered the Earth orbit to be circular, when they calculated the orbital elements. In Fig. 3a, we see that $\Delta\Omega$ of many showers acquires a value near $2°$ in two specific, relatively narrow intervals of Ω. When we construct the function $\Delta\Omega = \Delta\Omega(\Omega)$, whereby $\Delta\Omega$ is the difference of Ω calculated by considering the elliptical and circular Earth's orbit, then the curve showing the dependence (Fig. 3b) matches the sinusoid-like accumulation of points of many real showers. Two sinusoid-like curves correspond one to the showers colliding with the Earth in the ascending and second to the showers in the descending node of their orbit.

Another type is a simple typing error. An example of such an error was the value of the mean longitude of the ascending node in solution AdNo. 4 of the shower with the IAU No. 18 in the recent version of the MDC data. The value was equal to $321.1°$ (the second last line in Example 5 above). We see that the corresponding calculated value is $229.6°$, therefore numerals "2" and "3" were obviously interchanged in the published value. When the value of $321.1°$ is corrected to $231.1°$, none of the parameters of this solution are listed as incorrect in the file *errors_geo.inf* or *errors_orb.inf*. The mean longitude of the ascending
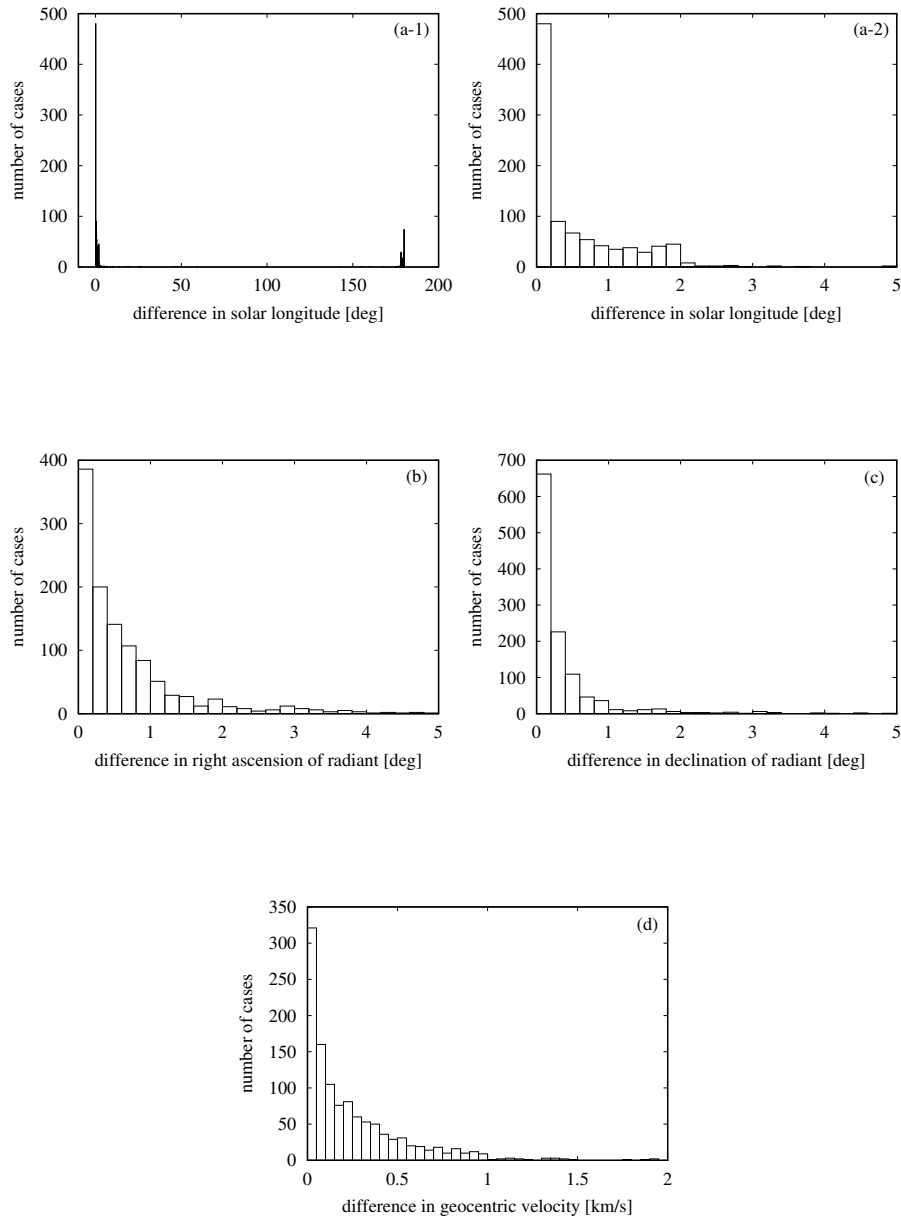
Figure 1. Distributions of absolute values of differences between the solar longitudes (panels a-1, a-2), right ascensions (b) and declinations (c) of geocentric radiants, and geocentric velocities (d) as given in the MDC list of showers (the version on January 11, 2023, with 1182 complete solutions) and calculated with the help of a program created within this work.
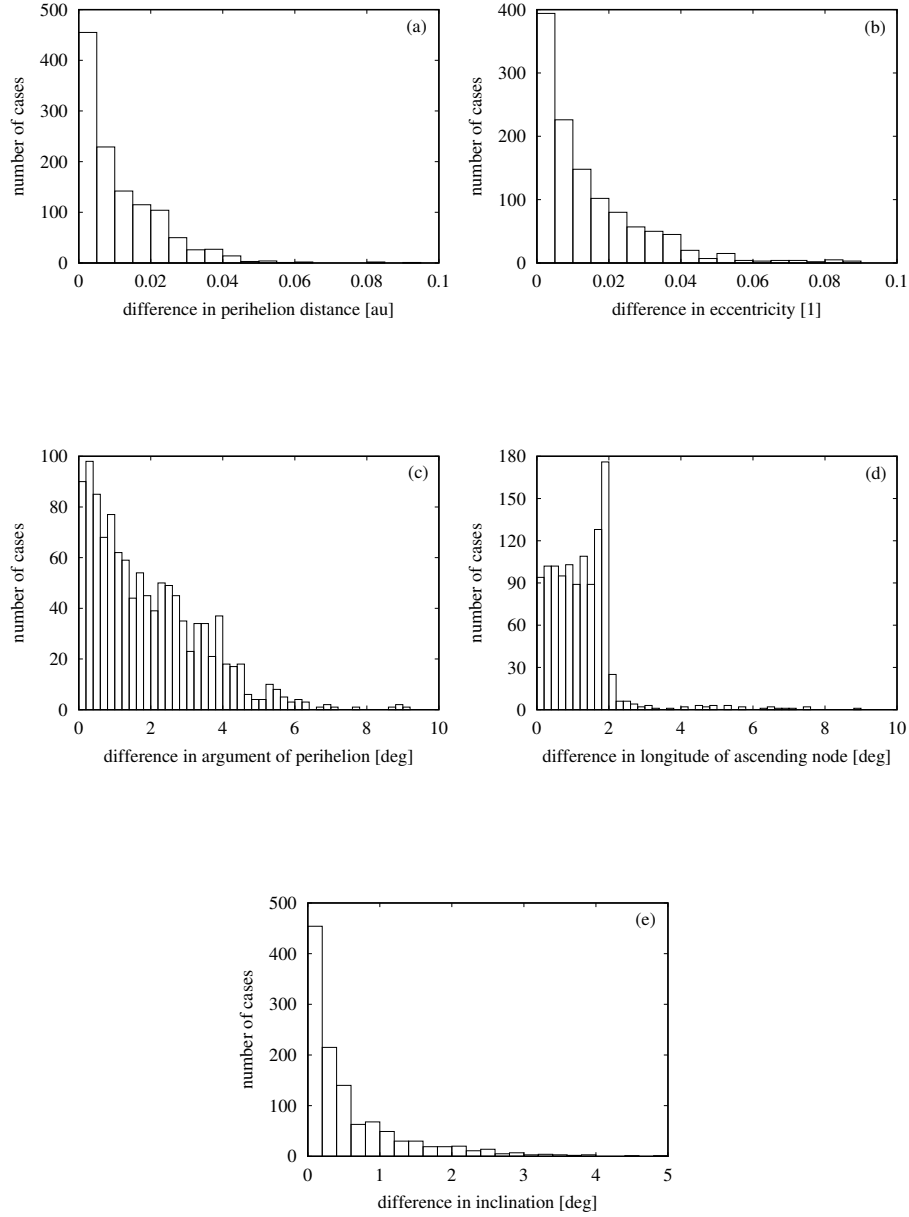
Figure 2. Distributions of absolute values of differences between the perihelion distances (panel a), eccentricities (b), arguments of perihelion (c), longitudes of ascending node (d), and inclinations (e) as given in the MDC list of showers (the version on January 11, 2023, with 1182 complete solutions) and calculated with the help of a program created within this work.
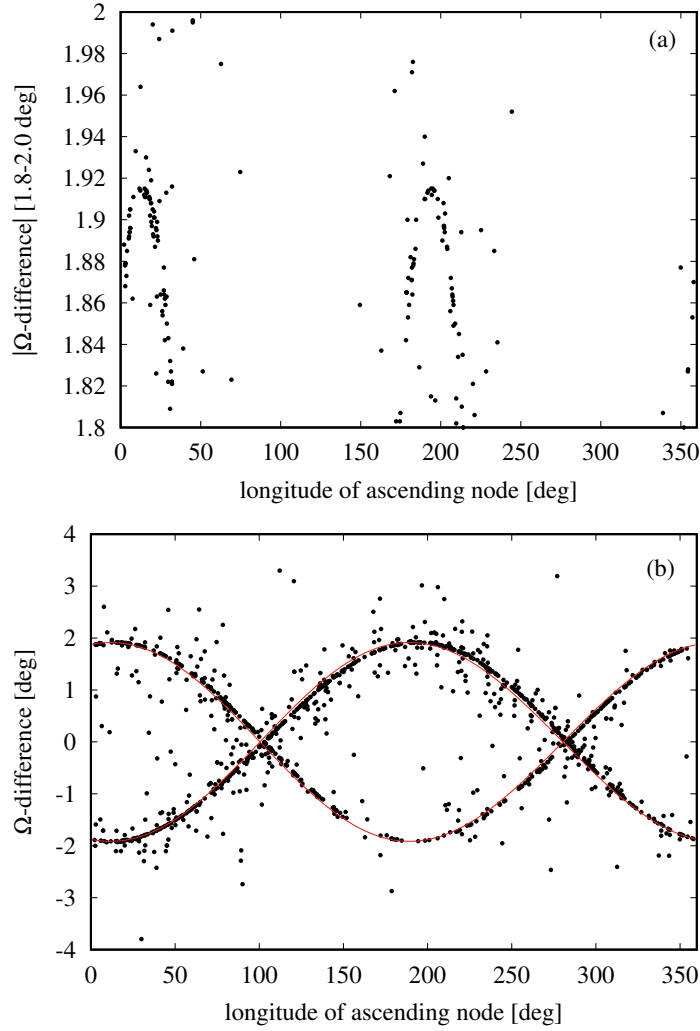
Figure 3. The figure to explain the reason for the highest peak in the distribution of the differences in longitude of ascending node, Ω, which is seen in Fig. 2d. In panel (a), the size of the difference of Ω in the interval from $1.8°$ to $2.0°$ (the highest peak in Fig. 2d) as the function of Ω is shown. This difference is more abundant in two specific intervals of this orbital element. In panel (b), there is shown the Ω-difference as depends on Ω in the interval $-4°$ to $+4°$ (black points). One can observe a twofold sinusoid-like behavior of the difference between many showers. The smallest derivative of these curves is just in the intervals of the peak. The red curves show the difference when Ω is calculated considering the true, elliptical, and circular orbits of the Earth. One curve corresponds to the showers colliding with our planet in the ascending and the other in the descending node of their orbit.

node is then consistent with the mean solar longitude of this solution, which equals just 231.1°. (The erroneous value was, meanwhile, corrected; the right value can be found on the current MDC website.)

In Fig. 1a-1, we can see quite a lot of differences in the solar longitude equal to ~180°. Obviously, the solar longitude was misidentified with the longitude of the Earth. A wrong identification of the quadrant can also occur at other angular parameters.

Some solutions are completely inconsistent. An example of such a solution is AdNo. 1 of the shower IAU No. 11. When its geocentric parameters are calculated using the program *radiants*, the large differences, above the tolerance limits, are found in the solar longitude, right ascension and declination of radiant (the second to fourth lines of Example 2 above). Using the program *elements* for the reverse calculation, one can find significant differences in perihelion distance, eccentricity, inclination, and argument of perihelion (the seventh to tenth lines of Example 5). The cause of the inconsistency in such a case is unknown.

The errors of the above-outlined types can occur due to a wrong determination of parameters (in the far past, the calculations were performed manually). Or, the inconsistency occurred due to a mistake when the data were re-written. The authors often create a table of geocentric data of showers and another table with their orbital elements. When merging these tables, the geocentric (orbital) parameters belonging to the previous or next showers in the table may be erroneously read and merged with the orbital (geocentric) parameters of the given shower. Of course, other reasons are not excluded.

5. Access to the software

The programs are freely accessible with this article, https://www.astro.sk/caosp/Eedition/FullTexts/vol54no1/pp57-71.dat/, and on the website of the IAU MDC[1], in the download section of the Shower Database part. In more detail, the Fortran77 source code of both programs, *radiants.f* and *elements.f* as well as the executable static binary codes, *radiants.exes* and *elements.exes*, are provided together with the template input and output data files. These files can be immediately run on the machines with the UNIX/Linux operation system. File *readme* with the description of the whole package is attached.

We recommend that researchers who deal with meteor showers use the programs and verify, in this independent way, the mutually dependent shower parameters.

---

[1]https://www.iaumeteordatacenter.org/

References

Hajduková, M., Rudawska, R., Jopek, T. J., et al., Modification of the Shower Database of the IAU Meteor Data Center. 2023, *A&A*, **671**, A155, DOI: 10.1051/0004-6361/202244964

Jopek, T. J. 1986, Comet and meteor streams associations, PhD thesis, Astronomical Observatory, Physics Department, A.M. University, Poznan, Poland

Jopek, T. J., Catalogue of precise meteor orbits. 1991, in *Dynamics of Small Bodies of the Solar System*, 49–54

Jopek, T. J., Valsecchi, G. B., & Froeschlé, C., Meteor stream identification: a new approach - III. The limitations of statistics. 2003, *Monthly Notices of the RAS*, **344**, 665, DOI: 10.1046/j.1365-8711.2003.06888.x

Koseki, M., Analysis of Meteor Data on a Microcomputer System. 1986, *Journal of the British Astronomical Association*, **96**, 232

Koseki, M., Research on the IAU meteor shower database. 2016, *WGN, Journal of the International Meteor Organization*, **44**, 151

Lindblad, B. A., The IAU Meteor Data Center in Lund. 1991, in Astrophysics and Space Science Library, Vol. **173**, *IAU Colloq. 126: Origin and Evolution of Interplanetary Dust*, ed. A. C. Levasseur-Regoud & H. Hasegawa, 311

Lindblad, B. A., Documentation of Meteor data availiable at the IAU meteor data center. 1992, in *Lund Observatory documentation*, ed. B. A. Lindblad

Lindblad, B. A., Neslušan, L., Porubčan, V., & Svoreň, J., IAU Meteor Database of photographic orbits version 2003. 2003, *Earth Moon and Planets*, **93**, 249, DOI: 10.1007/s11038-004-1953-4

Lindblad, B. A., Neslušan, L., Svoreň, J., & Porubčan, V., The updated version of the IAU MDC database of photographic meteor orbits. 2001, in ESA Special Publication, Vol. **495**, *Meteoroids 2001 Conference*, ed. B. Warmbein, 73–75

Neslušan, L., Porubčan, V., & Svoreň, J., IAU MDC Photographic Meteor Orbits Database: Version 2013. 2014, *Earth Moon and Planets*, **111**, 105, DOI: 10.1007/s11038-013-9427-1

Neslušan, L., Porubčan, V., Svoreň, J., & Schunová, E., New 211 photographic meteor orbits in the IAU MDC. 2012, *Contributions of the Astronomical Observatory Skalnate Pleso*, **42**, 85

Neslušan, L., Svoreň, J., & Porubčan, V., A computer program for calculation of a theoretical meteor-stream radiant. 1998, *Astronomy and Astrophysics*, **331**, 411

Rudawska, R., Hajdukova, M., Jopek, T. J., et al., Status of the IAU Meteor Data Center. 2021, *WGN, Journal of the International Meteor Organization*, **49**, 163

Southworth, R. B. & Hawkins, G. S., Statistics of meteor streams. 1963, *Smithsonian Contributions to Astrophysics*, **7**, 261

Svoreň, J., Porubčan, V., & Neslušan, L., Current Status of the Photographic Meteoroid Orbits Database and a Call for Contributions to a New Version. 2008, *Earth Moon and Planets*, **102**, 11, DOI: 10.1007/s11038-007-9167-1